SOLPS-ITER modeling of divertor scenarios for EU-DEMO

SOLPS-ITER modeling of divertor scenarios for EU-DEMO

To cite this article before publication: Fabio Subba *et al* 2021 *Nucl. Fusion* in press https://doi.org/10.1088/1741-4326/ac1c85

SOLPS-ITER Modeling of Divertor Scenarios for EU-DEMO

F. Subba

NEMO Group, Politecnico di Torino, Italy

E-mail: fabio.subba@polito.it

D. P. Coster

Max Planck Institute for Plasma Physics, Boltzmannstrasse 2, Garching bei Muenchen, Germany

M. Moscheni

NEMO Group, Politecnico di Torino, Italy

M. Siccinio

EUROFusion Consortium, and Max Planck Institute for Plasma Physics, Boltzmannstrasse 2, Garching bei Muenchen, Germany

February 2021

Abstract. We developed a first Single Null (SN) divertor scenario for EU-DEMO with the SOLPS-ITER code, including all charge states of D, He and Ar in the simulation and kinetic analysis of the neutral gas, but still leaving out drifts. Our results suggest that a partially detached divertor condition can indeed be obtained, with a corresponding peak heat flux on targets to $\approx 2\mathrm{MW/m^2}$, within the expected tolerable steady-state limits. The plasma re-attaches $\approx$ 30 cm (measured along the plate) from the Low Field Side (LFS) strike point deep in the SOL, with a consequent raise in the electron temperature up to $\approx$ 16eV outside the detached region, which requires further analysis to assess a possible role of sputtering, especially considering W self-sputtering. The plasma we developed exhibits $Z_{eff} \approx 1.9$ in the core, and a pumping speed a few hundred's $\mathrm{m^3/s}$ to maintain steady-state; this points to the need of further studies to better characterize the He accumulation in the core region.

1. Introduction

The baseline divertor scenario under consideration for EU-DEMO extends the solution developed for ITER [1], built around a standard SN magnetic topology. In the ITER case, the divertor is expected to operate in the high-radiation regime, where extrinsic impurities are injected to enhance dissipation up to $\approx$ 70% of P_{SOL}, so favoring detachment and reducing the heat target load to $\leq 5 - 10 MW/m^2$. In the case of EU-DEMO the ITER limits have to be considered only as upper estimates, at least with the current monoblock technology [2]. In fact, EU-DEMO will produce a large fluence of high-energy neutrons, and the divertor components should enjoy a long operational lifetime. This will most likely generate more severe requirements. To

further favor detachment, the baseline ITER-like scenario for EU-DEMO could possibly be substituted by more sophisticated alternative divertor solutions [3]-[4] for which, however, limited theoretical and experimental experience exists.

In addition to the limit on power density, sputtering is a further major concern for the target lifetime. This poses severe constraints on the electron temperature at the front of the target plate, which were preliminarily quantified as ($T_e < 5$ eV) [5].

A first analysis of possible EU-DEMO high radiating scenarios was presented in [6], still relying on a number of simplifying assumptions. Here we extend that work, relaxing some of its most constraining approximations. In particular, we developed the first analysis including: kinetic-neutrals, a realistic description of the first-wall geometry, and accounting independently for each charged species present in the plasma (assumed to be D+He+Ar). As discussed below, the atomic species for core radiation, namely Xenon [7], has not been included in the analysis. Also, the presence of intrinsic W has been neglected.

We show that, considering an Ar injection rate in the divertor of $1.5 \times 10^{19}\ s^{-1}$, it is possible to develop acceptable divertor conditions with a sufficiently low upstream density ($n_{up} \approx 2.8 \times 10^{19}\ m^{-3}$, corresponding to $\approx 0.42 n_G$). In such conditions, the core plasma shows a volume-averaged value of $Z_{eff} \approx 1.9$.

Our calculations predict a dissipation level by line radiation from ionized species of about 75 MW, corresponding to $f_{line,rad} = P_{line,rad}/P_{SOL} \equiv\sim 55\%$. To this, a considerable amount of power dissipated by neutrals should be added, needed to sustain the particle balance. In our simulation, 49 MW are associated to interactions with neutrals, raising the total dissipation to 91% of P_{SOL}. In the scenario developed, the heat load to the target does not seem to be a concern, being at most around $2MW/m^2$, including contributions from radiative load. Although the power density deposition limit for EU-DEMO is more demanding than for ITER, our calculated values still appear to comply with this requirement.

In our predicted scenario, temperature at the high-field-side (HFS) target and at the low-field-side (LFS) strike point are low enough to avoid W sputtering even considering the strict limit $T_e < 5$ eV. However, far from the LFS strike point the plasma re-attaches; the consequent increase of the electron temperature (up to ~ 16 eV) demanding further careful analysis. A rough estimate suggests it to be still manageable, thanks to the very low particle flux hitting the target in the high-temperature region. At this time, our data do not allow positive conclusions and more detailed simulations, possibly including W among the fluid species to allow for self-sputtering, will be required.

The paper is organized as follows. In section 2 we describe the main parameters of our target scenario, and the simulation setup; in section 3 we discuss the criteria adopted to our simulation actually reached steady-state; section 5 contains the main contribution of the paper: it describes a possible partially detached scenario for EU-DEMO , with an attempt to relate it to the currently accepted physical understanding of the process. Section 6 discusses at some length the role of Ar in the scenario we present, also pointing out the need for additional studies to better clarify it; in section

7 we introduce a very preliminary analysis of additional aspects which are not the focus of this paper, but should be included in a more comprehensive study. Finally, in section 8 we draw our conclusions and present some ideas for possible future developments.

2. EU-DEMO scenario and main simulation parameters

2.1. Domain and mesh

Figure 1a shows the profile of the EU-DEMO wall considered for this study (black solid line). For the sake of reference, some additional important elements are also shown: the location of the D_2 puff slot (magenta) at the outboard mid-plane (OMP), the pump slot (green) at the bottom of the divertor region, and the boundaries of the fluid mesh (black dotted lines). Figure 1b presents a magnification detail in the divertor region. It makes more visible details like the location of the Ar puff slot (red) just above the baffle of the low-field side (LFS) target, and the separatrix (blue). The fluid mesh, also shown in figure 1a, comprises 96 cells in the poloidal direction and 36 in the radial one. Previous studies suggest that this mesh should correspond to a residual discretization error $\lesssim 20\%$ induced by the finite cell-size [8]-[9].

2.2. Atomic physics

We run SOLPS-ITER activating the kinetic treatment of neutrals. At the cost of noticeable additional computational effort, this allows to include a realistic description of the wall geometry, a more precise location of the pumping and puffing slots, transport of neutral molecules and a rich wealth of atomic physics processes.

Table 1 lists the atomic physics reactions considered in our model. In order to give a feeling of their relative strength, the corresponding reaction rates are also shown in figures 2a-2c. In order to allow better reading of the data, we split the figures grouping together reactions involving atoms (figure 2a), neutral molecules (figure 2b) and molecular ions (figure 2c).

Data for reactions involving ionized species come from the adas database [10]. In particular, data for He reactions come from version adas96. For Ar, our code version consider adas89 for all rates except line radiation, which uses adas42.

2.3. Physical setup

The scenario considered corresponds to the EU-DEMO baseline 2018 [11]-[12], with $\sim$ 450 MW deposited in the core (alpha + auxiliary heating). The power entering the SOL should be as low as possible, still higher than the threshold level needed to maintain H-mode operation, estimated to be $P_{SOL,min} \sim 112$ MW [13]. The difference power should be radiated within the confined plasma region by the injection of a suitable core radiator impurity (possibly Xe). However, in the current study we did not focus on core processes, nor attempted to develop an integrated analysis yet. Consistently,

we did not consider the core radiator as an explicit SOL plasma component, but simply assumed it to act so as to lower the power input through the core boundary down to $P_{inp} = 150$ MW, including a safety margin to ensure H-mode operation. A dedicated SOL radiator will still be needed, most likely Ar [6]-[14], to avoid excessive target peak power levels; we included it explicitly in our modeling as well as He, in order to assess, at least preliminarily, its accumulation in the core plasma.

Based on these considerations, our model plasma is composed by D, Ar and He. As for the latter, we set its production to $\Gamma_{inp}^{He} = 7.1 \times 10^{20}\text{s}^{-1}$ at the core boundary, consistently with the expected fusion power $P_{fus} = 2$GW. We puffed Ar through the slot shown in figure 1b, at a rate of $\Gamma_{puf}^{Ar} = 1.5 \times 10^{19}\text{s}^{-1}$. We choose the latter value tentatively to provide a sufficient dissipation level in the SOL, and *a-posteriori* checked its compatibility with core conditions. Further studies would possibly lead to a better optimization of this parameter.

The fueling scheme under development for EU-DEMO predicts at least two main D sources dedicated to (i) fuel the core and keep a reasonably high central density, and (ii) sustain the SOL upstream density n_{up}. In our modeling, we included core fueling with a D volumetric deposition profile, as shown in figure 3. This corresponds to a gaussian shape centered ≈ 11 cm deep in the core, injecting $S_{core}^{D} = 7.0 \times 10^{21}$ s^{-1} atoms. The chosen source aims at mimicking (roughly) a pedestal fueling system acting via pellet injection. We note that precise details of the source are not important here, because other critical features of the core plasma (e.g. transport coefficients and pedestal width) were out of the scope of the present work, and we put little attention on them so far. Here we only mention that a preliminary scan on S_{core}^{D} suggested n_{up}, which in turn have a large influence on divertor conditions, to be relatively insensitive to it, at least if the core density is to be kept at physically reasonable values. Conversely, the deuterium puff level $\Gamma_{puf}^{D_2}$ influences significantly n_{up}, with limited effect on the core density, since the SOL ionizes very efficiently the neutral atoms, so preventing their penetration within the core. In this model we set $\Gamma_{puf}^{D_2} = 10^{23}\text{s}^{-1}$ (equivalent atomic flux), resulting in a steady-state value $n_{up} \approx 2.8 \times 10^{19}$ m^{-3}, still compatible with the requirements discussed in [15].

Figure 4 shows the transport coefficient profiles we assumed. They were chosen mainly to obtain a SOL power width $\lambda_E \approx 3(mm)$ at the OMP, which we tentatively assumed to be a reasonable value, combined with a very limited attempt to draft the formation of a core pedestal. It has to be noted that the actual SOL width value is largely uncertain. Estimates based on extrapolations from current experiments [16] or semi-quantitative heuristic models [17] would point out to millimetric or sub-millimetric size. On the other hand, recent gyro-kinetic calculations [18] suggest the actual value could be much larger, and more easily tolerable. Our choice correspond to a value somehow in the middle, small enough to pose severe power exhaust problems, but still manageable with a not exceedingly small radial cell-size.

2.4. Other boundary conditions

The physical setup described in the previous section involves some of the boundary conditions needed to perform the simulation. The complete set of boundary conditions implemented is obviously much larger. A weak point of our (as well as any other) modeling is that, in many cases, the physical information available to properly constrain the model is only a subset of the informations needed by the model to allow for a complete solution. Missing a better choice, we cover this lack of information by accepting the default boundary conditions proposed by the code during the case setup, or putting some values which experience shows to favor obtaining a numerically stable solution. Here we list our choices.

2.4.1. Core-boundary At the core boundary we assume a flux of D ions $\Gamma_D^+ = 5 \times 10^{20}$ s^{-1}. Note that this is not intended to compensate for the profile of the pellet injection profile cut as shown in figure 3. Much less ambitiously, it helps to stabilize the numerical procedure while not being strong enough to noticeably influence the final result. For all other particle species (except fully ionized He), we assume zero flux. Also, we impose that no parallel momentum enters the domain through the core boundary.

2.4.2. Targets At the target plates we consider standard Bohm-Chodura conditions for the parallel velocity and let the code adjust the electric potential through the current-voltage characteristics [19].

2.4.3. Wall boundaries As figure 1a shows, at all the solid-surface boundaries (except the targets) the fluid mesh does not extend up to the wall. This forces the user to select somehow ad-hoc conditions for the fluid plasma solver. At these boundaries we specify a decay length for the temperature and density profiles (3 cm) and a radially flat parallel velocity profile (i.e., no parallel momentum exchange at these boundaries). The mesh limitation does affect neutral atoms, which can reach the wall. A neutral hitting the wall (except at the pump location) is always reflected. The statistical distribution of the reflected particles is described by a standard database produced by the TRIM code [20]. Reflection details depend on the impinging species, wall material and temperature; we assume the wall to be made of W, with a temperature $T_{wall} = 0.1$ eV along the targets and $T_{wall} = 0.06$ eV elsewhere.

3. Steady-state assessment

For this study, we run SOLPS-ITER with both modules B2.5 and EIRENE for the ion and neutral transport, respectively. Since EIRENE is a Monte Carlo (MC) code, standard convergence criteria, usually adopted for purely fluid codes, may easily be never met, unless an un-realistically large number of (MC) test particles are followed to

keep the statistical noise at a negligible level. As a work-around, we assessed steady-state of our modeling as a combination of criteria based on residual evaluation for the fluid equations solved, visual inspection of time traces of significant quantities, and semi-quantitative assessment of their time-scale evolution. Figure 5 shows the time traces of global quantities, such as the total electron content (left axis), and electron and ion internal energy (right axis). The figure reports only the last 8×10^{-2} (s) of the transient evolution. The actual time needed for the plasma to evolve to steady-state depends obviously on the initial configuration. In the case we are considering, the actual evolution was much longer than what figures 5 and 6 would suggest. However, the previous part of the plasma history does not contain relevant information to assess the steady-state, and we do not show it.

In addition to inspecting visually the steadyness of the traces, we also evaluate the characteristic evolution time at the end of the simulation as

$$\tau_X = \frac{X_1 + X_2}{2} \left| \frac{t_2 - t_1}{X_2 - X_1} \right| \tag{1}$$

where X_i is the quantity we are checking, averaged over 100 time steps (to smooth-out MC noise) around time t_i. In order to reduce possible correlation of the values tested at the times t_i, it is obviously preferable that $100dt \ll |t_2 - t_1|$; in the case under consideration we have $dt = 10^{-6}$ s, and $|t_2 - t_1| = 10^{-2}$ s. From the legend in figure 5 we see that all evolution times are above a minimum value of 10 s, sufficiently long compared to a characteristic evolution time estimated as L/c_s . Evaluating the connection length from the outer mid-plane to the outer target gives an average value of ≈ 118 m (taken over the first 6 poloidal cell rings adjacent to the separatrix in the SOL, corresponding to a radial distance of about 3.3 mm from the separatrix at the OMP). Assuming a characteristic temperature of 100 eV for both ions and electrons then gives $L/c_s \approx 1.2$ ms. Other evolution times can be estimated, for each species, as $\tau = N/S$, with N the total species content in the computational domain and S the particle source (either flux from the core, in the case of He, or gas puff for D and Ar) [21]. In our case, the corresponding times are 0.14 s (for D), 3.3 s (for He) and 2.8 s (for Ar).

Comparing these values with the observed evolution rates determined using equation (1) above is not trivial, since they are artificially modified by the implementation of some acceleration techniques. In particular, in the core region (often found to be the slowest one to evolve), we run with a time step artificially increased by a factor 10^3. Moreover, we enabled the method of effective source as described by [21]. All acceleration schemes implemented would, during a transient, introduce non-physical features. However, they are designed in such a way that their effect on the final steady-state cancels out. A precise assessment of the evolution times when the acceleration schemes are taken into account is difficult, and out of the scope of this paper. We simply observe that their effect is usually to shorten the transients by at least an order of magnitude, which allows us concluding that our case is safely steady.

In addition to this, figure 6 shows the evolution of some *local* quantities: the maximum electron density and temperature at the targets. Characteristic evolution

times evaluated for such traces have values ≈ 1 s. Since they are evaluated at specific locations, we are not surprised to find them shorter than the previous global traces; still they appear to be sufficiently larger than the characteristic evolution times.

4. Divertor conditions overview

In this section we will provide a global overview of divertor conditions as expected by our modeling, to give the reader an introductory knowledge of our expected scenario and to facilitate later referencing. Figures 7a and 7b show the electron and ion temperature in the divertor region. Data are represented using a logarithmic scale, to allow appreciating the details of the map spanning a data range several decades wide. Electron and ion maps suggest divertor detachment takes place at the HFS target (T close to 1 eV), while at the LFS the temperatures increase noticeably leaving the separatrix towards the far SOL. We will discuss this better in section 5 later. Also, both maps show a single cell with very low temperature close to the LFS strike point in the PFR. There is no physical reason for such a localized anomalous value, which we assess to be due to imperfect numerical convergence. The feature is responsible for localized perturbation in the profile of some quantities sometimes noticeable at the targets where the offended flux tube strikes the solid wall (see e.g. later, figure 10b). However, we could not detect a global influence on the modeling result and consequent discussion. We feel that we can safely accept this imperfection. Figures 7c and 7d show the atomic and molecular temperatures in the divertor region. D atoms can be heated up to temperatures of several eV by CX with ions (the few atoms penetrating in the main SOL of the core can be even hotter), while molecules, for which CX with ions is much less likely to happen, stay colder, especially close to the divertor bottom.

Figures 8a and 8b show the electron and molecular density in the divertor region. At both strike points the n_e is considerably large, as expected in high recycling regime close to detachment. We will analyze this in more detail in section 5. Also the molecular density is large in the PFR region, the exact value being determined by an interplay of recycling processes and pumping (the pump duct entrance is marked by the thick green line on the divertor bottom). Notice that the pattern of molecular density in the main SOL is strongly un-physical, presenting variations of a few orders of magnitude between adjacent cells. This is a feature originating from the statistical noise introduced by the Monte Carlo neutral solver, which is amplified in the SOL where only a few test-molecules can penetrate. On the other hand, such feature appears where the molecular density in the main SOL is very low so that, on practical terms, we can assume it to be simply zero and neglect the observed oscillations.

5. Detachment analysis

For EU-DEMO to comply with the steady-state requirements listed in section 1, it is commonly understood that detached conditions will be necessary along most, if not all,

of the divertor target surface. This, in turn, requires a considerable fraction of P_{SOL} to be radiated and, at the same time, a relevant reduction of the total plasma pressure in the divertor region, mostly operated by CX reactions [22]. Figures 9a and 9b show the electron temperature and density profiles along the Low Field Side (LFS) and High Field Side (HFS) targets, respectively. The HFS temperature is uniformly below 3.5 eV. Such low values are usually associated with deep detachment and should not imply any concern in tems of sputtering. Instead, at the LFS target, where ≈ 30 cm away from the strike point T_e reaches a noticeable maximum value ≈ 16 eV, which could raise some concern [5].

The power load to the target, per se, does not seem to be a major concern. Figure 10a and 10b show the power deposition profile along the targets, highlighting contributions related to different physical mechanisms. Consistently with the generically low temperature along the targets, the dominant contribution is due to the energy released by surface recombination processes [22]. On the HFS, where detachment is deeper, a significant contribution comes also from neutrals radiation caused by interaction with electrons before ionization can actually take place. It is true that, at the LFS, far from the strike point the temperature increases noticeably, but in this region the electron density is low enough to result in a globally reduced level of the heat flux $q_E \propto n_e T_e^{3/2}$, although in correspondence of the T_e maximum a flattening of the heat flux profile is clearly visible (compare figures 9b and 10b).

To obtain detachment, a considerable fraction of the plasma momentun should be removed through CX reactions. This is shown in figures 11a and 11b, comparing the total pressure at the divertor entrances with with the values at the targets. From basic 2 point model analysis [19], the two quantity should roughly match for attached plasmas. The drop at the targets clearly indicates that the HFS target is fully detached, while the LFS only partially. For the sake of reference, in figure 11b we also marked the position of the maximum power deposition (the black dashed line), taken from figure 10b above. This makes apparent how the most loaded region is where plasma transitions from detached to fully attached. An intermediate high-recycling region develops with very large ion flux to the wall. The large power deposition associated with recombination within the solid structure is the most important load contribution.

In order to allow CX reactions to remove a sufficient amount of momentum from the plasma, the temperature should first drop down to a few eV, which usually requires strong power dissipation from line radiation and recycling. Figure 12 shows the distribution of radiative dissipation in the divertor region. The total line radiation from ionized species amounts to 75 MW, to which another 49 MW of dissipation associated to interactions with neutrals should be added. This reduces the power deposited onto the targets down to ≈ 9 MW at the HFS target and ≈ 21 MW at the LFS one, corrseponding to the tolerable peak values reported in figures 10a and 10b. The power diverted away from the targets through radiative processes distributes onto the first wall and divertor bottom. Although radiative power is likely to distribute relatively uniformly on the walls, it should still be monitored, since away from the targets the wall cannot be

strongly armored in order not to compromise the reactor tritium breeding ratio. A post-processing estimate gave peak values smaller than 300 kW/m^{-2} and 220 kW/m^{-2} on the divertor and main wall, respectively..

The interplay between radiation, CX and elastic collisions to favor detachment is highlighted in figures 13a and 13b. They present an analysis of various quantities taken along a detached flux tube (radially $\approx$ 1cm away from the separatrix, measured at the OMP), focusing on the last meter before hitting the LFS target. In figure 13a, we selected the electron temperature (because of its large influence on the reaction rates) and the total pressure (evaluated summing up the ion and electron static pressures, and the plasma kinetic energy density $\sum_i n_i m_i v_i^2/2$), which we take as the main detachment indicator. In figure 13b we show the density of CX and elastic collision events (evaluated by multiplying the reaction rates evaluated at the local plasma conditions by the reactant densities), and the power density dissipated by radiation. Comparing the two figures makes it clear that line radiation, by itself, is not sufficient to trigger the pressure reduction, which stays relatively large in the region of strong radiation. However, line radiation does contribute to lower the temperature to a level at which CX and elastic collision rates increase significantly and trigger detachment. Comparison of CX involving atomic and molecular D as neutral species also suggests that the molecular CX channel does not play a direct role in the plasma momentum removal process.

Careful analysis of the energy balance shows that the output power from the system seems to be actually larger than the input. For example, summing-up dissipation and targets leads to $\approx$ 154 MW power output. We estimate that most of this inconsistency is due to a non-perfect convergence of the energy equations. Residual analysis reveals oscillations which can be in the range 0-4 MW for electrons and 0-1 MW for ions. Such oscillations are most evident in the outer divertor region. From one side, we believe that observing possible numerical problems arising in a region where a wealth of non-linear physics becomes important should not be surprising. On the other hand, the total residual imbalance is relatively small (but still compatible with the observed level of energy non-conservation), and we estimated that obtaining a more accurate solution would have require much effort (mostly in terms of numerical parameters setting), without returning a correspondingly large improvement of the solution quality.

Figure 9b suggests that the plasma in the far LFS SOL can still be attached, with relatively high electron temperature. This might be a concern for sputtering processes, as we will discuss later, and it is worth trying to make an estimate of what could determine this distance. Our previous discussion suggests that in order to detach a flux tube we need both (i) sufficiently high plasma density (to lower the target temperature) and (ii) large neutral density to drive CX momentum removal. The two conditions are usually coupled, because neutrals originate from the ions being absorbed at the wall and recycling. We assume a neutral emerging from the target will undergo an effective diffusion process driven by CX reactions. We estimate the associated diffusion coefficient as

$$D \approx v_{th}^2 \tau_{CX} \tag{2}$$

with v_{th} the particle thermal velocity and $\tau_{CX} = \left(\langle\sigma v\rangle_{CX} n_i\right)^{-1}$. The neutral atom can survive before ionizing a time $\tau_{ion} = \left(\langle\sigma v\rangle_{ion} n_e\right)^{-1}$ so that we can expect it to depart from its originating location by a distance

$$l \approx \sqrt{D\tau_{ion}} \tag{3}$$

If we further assume $n_e \approx n_i$ and $v_{th} = \sqrt{2T/m}$ we obtain:

$$l \approx v_{th}\sqrt{\tau_{CX}\tau_{ion}} \propto 1/n_e \tag{4}$$

Taking indicative values of $n_e = 10^{20}\mathrm{m}^{-3}$ and $T_e = T_i = T_n = 5eV$ we get a diffusion distance $l \approx 3cm$. Although these numbers are just rough estimations, they suggest that comparatively few neutrals can fly as far as ≈ 10 cm away from the region of large target fluxes, which is roughly in agreement with the profiles shown in figure 9b.

We close this section by recalling that in our analysis we set SOL transport coefficients with the only constraint to provide a mid-plane power decay length of $\approx$ 3mm. Actual benchmark of edge modeling with experimental observation show that often the far SOL is strongly turbulent, requiring transport coefficients much larger than our guess, far from the separatrix [23]-[24]. Adopting similar transport coefficients in our model would possibly result in a slower decay of the density profiles in the far SOL, as well as lower peak values. However, we cannot say at the moment if and how effectively this would contribute to lower the temperature far in the SOL and extend the detached region. Such an effect could be the object of a later dedicated study.

6. Influence of Ar in the SOL and the core

As already discussed in section (2.3), we did not include a careful analysis of core conditions in the present study. It might still be useful to provide a brief sketch of what influence from Ar we can expect on the overall reactor energy balance. Figure 14 shows the electron and ion temperature radial profiles taken at the outer mid-plane. The maximum T_e in our simulation, observed at the inner core boundary, is slightly larger than 5 keV. Ions, which are not directly cooled-down by radiation processes but transfer their internal energy to electrons through collisional processes, are a few hundreds eV hotter.

The maximum electron temperature observed in our modeling is larger than the innermost electron extraction potential for Ar ($\approx$ 4.4 keV), although not exceedingly. In addition to the electron temperature, also ion transport can influence the charge states distribution, since ions penetrate in the core from low temperature external regions. As a consequence, we cannot predict a-priori Ar to be fully ionized at the inner core boundary of our modeling domain. In fact, figure 15, showing the relative distribution of Ar charge states at the core boundary, demonstrates that fully ionized Ar is the leading charge state, but other high-charge values are not completely negligible. However, we feel safe to assume that, with deeper core penetration, Ar^{18+} will quickly become the only charge state noticeably present, from which we conclude that the radiation contribution from Ar in the confined plasma is almost completely taken into account in our model (apart

from different possible density profiles arising from more accurate transport modeling).

The total Ar line radiation from the core (summed over all ionic charge-states) is about 3.5 MW. From the previous discussion, we do not expect this quantity to increase significantly, even if a larger core fraction were included in the model. Since $\geq$ 300MW are expected to be radiated from the core, it is clear that a different core radiator, like e.g. Xe, will ultimately be required.

Given the importance of Ar radiation in the detachment triggering process, it would be interesting to assess the sensitivity of the scenario analyzed to the Ar injection level. At present, a detailed scan on Ar puff rate including kinetic neutrals is not yet available, so that we cannot present a quantitative discussion. However, we can produce some considerations based on a series of runs produced on the same target geometry and input power level, although employing the fluid neutral model. These cases are part of an ongoing independent study, focusing on the comparison of different possible divertor geometries [4], [25]. A direct comparison with the results discussed in this paper is not possible; however, we believe that some qualitative considerations can be safely produced. Figures 16a-16c show the main result of a scan in Ar puff level, repeated at three different D fueling rates. Independently on the D fueling rate selected, we can observe a qualitatively similar behavior. At low Ar puff, the upstream density is relatively large (even un-realistically large), since a considerable amount of power is available to sustain ionization of the recycling fuel, see figure 16a. However, such upstream density, by itself, is not capable to trigger divertor detachment, and the target temperature stays large (figure 16b). When a significant amount if Ar is injected, less power is available to sustain ionizations, the upstream density drops as well as the target temperature. After some threshold level, the upstream density saturates as well as the total line radiation, which can also slightly decrease (figure 16c). This usually correspond to detached plasma, as can be inferred from figure 16b. This plateau is sustained by a complex balance between power available for ionization and radiation: increasing the Ar level leads to too large radiation, dropping the rate of ionization events. However, the same process hinders the possibility to accumulate a large amount of Ar ions, with a negative feed-back on the radiative level itself. Numerically we observe that, if we try to further increase the Ar puff level we cannot obtain anymore a converged plasma solution. We believe that this limit should be the numerical counterpart of the plasma collapse observed experimentally at very low power input levels, as in [26]. The amount of power radiation at which this saturation occurs varies with the D fueling rate; in the results presented here the threshold is located between $\approx$ 110 and $\approx$ 120 MW (figure 16c), corresponding to $\approx$ 73% and $\approx$ 80% of the total input power.

As already mentioned, establishing a precise correspondence between the behavior described in figures 16a-16c and the main case described in this paper is not easy. However, comparing the line radiation level and the maximum outer target electron temperature discussed in section 5, we speculate that our case could lie slightly before the plateau. The main features which suggest us this tentative conclusion are the

existence of a still relatively large target temperature, see figure 9b, and a not extremely large radiation level. We think it safe not to draw further conclusions from this limited comparison, and leave a more detailed study of the sensitivity of the scenario to the level of Ar supply to a future work.

7. Additional analysis

The main focus of this first work is the development of a detached divertor scenario for EU-DEMO. Consequently, the analysis of the underlying processes took a considerable time. However, our long-term goal is to evolve towards an integrated scenario, where other critical questions, like sputtering, pumping capabilities and coupling with core conditions will be treated in a consistent way. In the following, we illustrate the first implication of our current results with respect to such additional points.

7.1. Sputtering

Neither sputtering processes nor W are included in our modeling. This was done in order to save CPU time, because following all the 74 charge states of W would have increased considerably the time required for our computations. Moreover, a deep analysis of sputtering, impurity transport processes and their effect on the first wall would require probably a coupled study with a dedicated code such as, for example ERO2.0 [27]. In order to gain a first feeling about the importance of sputtering for the case at hand, we can still post-process the plasma we obtained to determine which sputtering level would correspond to the computed particle fluxes impinging on the target plates. Such calculations were performed using the TRIM database [28]. Figure 17a shows the estimated sputtering flux on the HFS and LFS targets. The figure does not give the detail of the various ionic species contributions, but it is largely dominated by Ar. Sputtering on the LFS target is by far the most significant (we actually multiplied the values on the HFS by a factor of 5 to allow appreciating them on the figure scale), as a consequence of the relatively large electron temperature. The maximum value is $\approx 6.3 \times 10^{17}\mathrm{m}^{-2}\mathrm{s}^{-1}$.

The value estimated here seems to be tolerable if compared with the limiting value $\Gamma^{sputt} \leq 1.5 \times 10^{19}\mathrm{m}^{-2}\mathrm{s}^{-1}$, reported in [5]. However, it should be noticed that it represents a largely rough estimate. Sputtering yields are extremely sensitive to the electron temperature in front of the target, on which our modeling still contains a relatively large number of uncertainties. Moreover, the sputtered flux is dominated by ions deeply ionized, as is clear from figure 17b. In fact, only the logarithmic scale allows appreciating that some sputtering at all takes place for all but the two most ionized charge-states, with Ar^{17+} a clear winner, in spite of the actual flux on the target of such ions being almost negligible. Sputtering from all other charge states can be classified as numerical noise. For these reasons, we believe that a more detailed study should require including W (capable of easily generate high charge-states) as an additional

atomic species in the model. Moreover, an analysis with a specifically dedicated tool like, e.g., the ERO code is also desirable as an extension of this work.

7.2. Impurity accumulation and pumping

The main requirements on pumping are connected to the capacity to remove efficiently He produced by fusion reactions, ultimately keeping the core plasma clean enough (i.e. maintainingh the He density sufficiently low to avoid dilution). Figure 18 shows the density profiles for the various species taken at the OMP (He and Ar values are summed over all ionic charge states). As a measure of the overall core pollution level we report the value $Z_{eff} \approx 1.9$. Individual impurities contributions are ≈ 0.58 for He and ≈ 0.75 for Ar, even if we should remember that Xe and W, which can heavily contribute to Z_{eff} by virtue of their large atomic mass, have been disregarded. Although this is not critically large, it still corrseponds to undesirable impurity concentration levels in the core plasma. On the other hand, we should remember that no attempt has been done, so far, to model realistically transport and accumulation of impurities in the core, so that the question will deserve further analysis in the future. Also related to the plasma particle balance is the analysis of the density developing in the divertor region, necessary to sustain the detached state which, in turn, influences the performance of the pumping system. Figure 8b shows the neutral D_2 density in the divertor region, which is close to $10^{21}\mathrm{m}^{-3}$ in the proximity of the pump duct opening (the green line at the bottom of the figure). This, combined with a D puff equivalent to 10^{23}atoms/s, corresponds to a pumping speed of several hundreds m^3/s. With favorable divertor conditions, such value looks technologically feasible [29]. On the other hand, a recent study accounting in detail the divertor profile analyzed in this paper suggests that the required particle exhaust could be hardly achieved with this divertor design, and points to the need of a dome to favor neutral compression and throughput [30].

8. Conclusions and perspectives

In this paper we described a first modeling performed with SOLPS-ITER of the EU-DEMO SOL and divertor plasmas, including D, He and Ar, and a kinetic treatment of neutral gas transport. The model focused on the possibility to obtain a detached plasma compatible with divertor acceptable lifetime, from the point of view of target heat load and Ar induced sputtering. Our results suggest that it should be possible to operate EU-DEMO at sufficiently low target heat load by dissipating $\approx 76\%$ of the power entering the SOL via line radiation (mostly from Ar) and recycling processes. This condition corresponds to upstream plasma density $n_{up} \approx 2.8 \times 10^{19}\mathrm{m}^{-3} \approx 0.42 n_G$. If we take tentatively the limiting value $n_{up} \leq 0.5 n_G$, a limited margin appears to be still available, if needed, to increase n_{up} in order to improve divertor conditions.

Despite not specifically aiming at this, we did a preliminary analysis of core conditions and neutral presence in the divertor. In this analysis He and Ar shows a

slightly large concentration level in the core. This aspect should be further analyzed in a future activity, possibly with the inclusion of a better neoclassical transport description in the confined plasma region.

The analysis we presented can obviously be improved along several directions. Among others, it is certainly worth mentioning i) the inclusion of W in a future model, which will allow a much more precise assessment of sputtering importance, ii) a systematic parametric study of the divertor shape, impurity mix composition and injection rate. The sketchy divertor profile currently available is not likely to be the final one, and its optimization (possibly including additional structures like, e.g., a dome) could be effective in favoring neutral compression and plasma detachment, and iii) an analysis of the effects of drifts on divertor conditions. In fact, although drift effect are favored by small machine size and strong gradients (i.e. mostly attached conditions), recent ITER modeling shows that drifts can change the divertor operational window to higher neutrals pressures [31]. All of this will be part of more extensive studies to come.

Finally, it is also noteworthy that a considerable fraction of the power load on the divertor and wall is due to radiative transport processes. In our modeling we did the quite simple assumption of optically thin plasma. Should the plasma present a short optical depth, the deposition pattern would likely change. Since the radiative source in our case is mostly concentrated close to the target, we expect that the additional diffusion process introduced by photon-matter collisions would likely not result in the creation of dangerous hot spots on the targets itself. However, at the current stage we cannot make any educated guess on what the load deposition redistribution would cause on the main wall and divertor. A photon transport module were included in the past in the EIRENE code [32]; however this model is now not active in the SOLPS-ITER 3.0.6 version used to prepare the present paper. As far as the authors know, an activity is ongoing to re-activate such model in future SOLPS-ITER versions, which would make such calculation possible.

The results presented in this paper were produced based on a number of SOLPS-ITER runs. The code version used is 3.0.6. The runs post-processed to produce the data shown are stored in the publicly available MDSPlus database. Table 2 lists all the runs, with their MDSPlus identifier.

9. Acknowledgment

The authors are grateful to Prof. V. Rozhansky and his group for valuable discussions on the draft and, in particular, for pointing us out a mistake in the figure reporting the He ionization reaction rates.

This work has been carried out within the framework of the EUROfusion Consortium and has received funding from the Euratom research and training programme 2014-2018 and 2019-2020 under grant agreement No 633053. The views and opinions expressed herein do not necessarily reflect those of the European Commission.

10. Bibliography

[1] R. A. Pitts, X. Bonnin, F. Escourbiac, H. Frerichs, J. P. Gunn, T. Hirai, A. S. Kukushkin, E. Kaveeva, M. A. Miller, D. Moulton, V. Rozhansky, I. Senichenkov, E. Sytova, O. Schmitz, P. C. Stangeby, G. De Temmerman, I. Veselova, and S. Wiesen. Physics basis for the first ITER tungsten divertor. *Nuclear Materials and Energy*, 20:100696, aug 2019.

[2] Muyuan Li and Jeong-Ha You. Interpretation of the deep cracking phenomenon of tungsten monoblock targets observed in high-heat-flux fatigue tests at 20 MW/m 2. *Fusion Engineering and Design*, 101:1–8, 2015.

[3] G. F. Nallo, S. Carli, G. Caruso, F. Crisanti, G. Mazzitelli, L. Savoldi, F. Subba, and R. Zanino. Modeling the lithium loop in a liquid metal pool-type divertor. *Fusion Engineering and Design*, 125:206–215, dec 2017.

[4] F. Militello, L. Aho-Mantila, R. Ambrosino, T. Body, H. Bufferand, G. Calabro, G. Ciraolo, D. Coster, G. Di Gironimo, P. Fanelli, N. Fedorczak, A. Herrmann, P. Innocente, R. Kembleton, J. Lilburne, T. Lunt, D. Marzullo, S. Merriman, D. Moulton, A. H. Nielsen, J. Omotani, G. Ramogida, H. Reimerdes, M. Reinhart, P. Ricci, F. Riva, A. Stegmeir, F. Subba, W. Suttrop, P. Tamain, M. Teschke, A. Thrysoe, W. Treutterer, S. Varoutis, M. Wensing, A. Wilde, M. Wischmeier, and L. Y. Xiang. Preliminary analysis of alternative divertors for DEMO. *Nuclear Materials and Energy*, 26:100908, 2021.

[5] R. P. Wenninger, M. Bernert, T. Eich, E. Fable, G. Federici, A. Kallenbach, A. Loarte, C. Lowry, D. McDonald, R. Neu, T. Ptterich, P. Schneider, B. Sieglin, G. Strohmayer, F. Reimold, and M. Wischmeier. DEMO divertor limitations during and in between ELMs. *Nucl. Fusion*, 54(11):114003, nov 2014.

[6] F. Subba, L. Aho-Mantila, D. Coster, G. Maddaluno, G. F. Nallo, Bernard Sieglin, Ronald Wenninger, and Roberto Zanino. Modelling of mitigation of the power divertor loading for the EU DEMO through ar injection. *Plasma Physics and Controlled Fusion*, 60(3):035013, feb 2018.

[7] R. Wenninger, R. Albanese, R. Ambrosino, F. Arbeiter, J. Aubert, C. Bachmann, L. Barbato, T. Barrett, M. Beckers, W. Biel, L. Boccaccini, D. Carralero, D. Coster, T. Eich, A. Fasoli, G. Federici, M. Firdaouss, J. Graves, J. Horacek, M. Kovari, S. Lanthaler, V. Loschiavo, C. Lowry, H. Lux, G. Maddaluno, F. Maviglia, R. Mitteau, R. Neu, D. Pfefferle, K. Schmid, M. Siccinio, B. Sieglin, C. Silva, A. Snicker, F. Subba, J. Varje, and H. Zohm. The DEMO wall load challenge. *Nuclear Fusion*, 57(4):046002, 2017.

[8] F. Subba. Simulations of sol plasmas in demo. https://idm.euro-fusion.org/?uid=2ms27p.

[9] K. Ghoos, P. Brner, W. Dekeyser, A. S. Kukushkin, and M. Baelmans. Grid resolution study for b2-EIRENE simulation of partially detached ITER divertor plasma. *Nuclear Fusion*, 59(2):026001, 2018-12.

[10] H. P. Summers. *The ADAS User Manual, version 2.6. https://www.adas.ac.uk*, 2004.

[11] J. Morris. Process input/output for the physics and magnet baseline august 2018 run https://idm.euro-fusion.org/?uid=2mkzul.

[12] M. Siccinio, W. Biel, M. Cavedon, E. Fable, G. Federici, F. Janky, H. Lux, F. Maviglia, J. Morris, F. Palermo, O. Sauter, F. Subba, and H. Zohm. DEMO physics challenges beyond ITER. *Fusion Engineering and Design*, 156:111603, 2020-07.

[13] Y. R. Martin, T. Takizuka, and the ITPA CDBM H-mode Threshold Data Group. Power requirement for accessing the h-mode in ITER. *J. Phys.: Conf. Ser.*, 123:012033, 2008.

[14] A. Kallenbach, M. Bernert, R. Dux, L. Casali, T. Eich, L. Giannone, A. Herrmann, R. McDermott, A. Mlynek, H. W. Mller, F. Reimold, J. Schweinzer, M. Sertoli, G. Tardini, W. Treutterer, E. Viezzer, R. Wenninger, and M. Wischmeier. Impurity seeding for tokamak power exhaust: from present devices via ITER to DEMO. *Plasma Physics and Controlled Fusion*, 55(12):124041, nov 2013.

[15] T. Eich, R. J. Goldston, A. Kallenbach, B. Sieglin, and H. J. Sun. Correlation of the tokamak

h-mode density limit with ballooning stability at the separatrix. *Nuclear Fusion*, 58(3):034001, 2018-01.

[16] T. Eich, B. Sieglin, A. Scarabosio, W. Fundamenski, R. J. Goldston, and A. Herrmann. Inter-ELM power decay length for JET and ASDEX upgrade: Measurement and comparison with heuristic drift-based model. *Physical Review Letters*, 107(21):215001, nov 2011.

[17] R. J. Goldston. Heuristic drift-based model of the power scrape-off width in low-gas-puff h-mode tokamaks. *Nucl. Fusion*, 52(1):013009, dec 2011.

[18] C. S. Chang, S. Ku, A. Loarte, V. Parail, F. Kchl, M. Romanelli, R. Maingi, J.-W. Ahn, T. Gray, J. Hughes, B. LaBombard, T. Leonard, M. Makowski, and J. Terry. Gyrokinetic projection of the divertor heat-flux width from present tokamaks to ITER. *Nuclear Fusion*, 57(11):116023, aug 2017.

[19] P. C. Stangeby. *The Plasma Boundary of Magnetic Fusion Devices*. Institute of Physics Publishing, 1999.

[20] W. Eckstein and D. B. Heifetz. Data sets for hydrogen reflection and their use in neutral transport calculations. *Journal of Nuclear Materials*, 145-147:332–338, 1987-02.

[21] E. Kaveeva, V. Rozhansky, I. Senichenkov, I. Veselova, S. Voskoboynikov, E. Sytova, X. Bonnin, and D. Coster. Speed-up of SOLPS-ITER code for tokamak edge modeling. *Nuclear Fusion*, 58(12):126018, oct 2018.

[22] S. I. Krasheninnikov, A. S. Kukushkin, and A. A. Pshenov. Divertor plasma detachment. *Physics of Plasmas*, 23(5):055602, may 2016.

[23] Wouter DEKEYSER, Xavier BONNIN, Steven W. LISGO, Richard A. PITTS, Dan BRUNNER, Brian LABOMBARD, and Jim L. TERRY. SOLPS-ITER modeling of the alcator c-mod divertor plasma. *Plasma and Fusion Research*, 11(0):1403103–1403103, 2016.

[24] F. Reimold, M. Wischmeier, S. Potzel, L. Guimarais, D. Reiter, M. Bernert, M. Dunne, and T. Lunt. The high field side high density region in SOLPS-modeling of nitrogen-seeded h-modes in ASDEX upgrade. *Nuclear Materials and Energy*, 12:193–199, 2017-03-09.

[25] L. Xiang, F. Militello, D. Moulton, F. Subba, L. Aho-Mantila, D. Coster, M. Wensing, T. Lunt, M. Wischmeier, and H. Reimerdes. The operational space for divertor power exhaust in DEMO with a super-x divertor. *Nuclear Fusion*, 61(7):076007, 2021.

[26] B. Lehnert, J. Bergstrm, M. Bures, S. Holmberg, and E. Tennfors. The minimum-power effect of a magnetized plasma. *Physica Scripta*, 9(2):109–118, 1974-02.

[27] A. Gallo, A. Sepetys, J. Romazanov, Y. Marandet, S. Brezinsek, H. Bufferand, G. Ciraolo, Y. Corre, S. Ertmer, N. Fedorczak, J. Gunn, A. Kirschner, C. Martin, O. Meyer, G. J. van Rooij, P. Roubin, and E. Tsitrone. First efforts in numerical modeling of tungsten migration in WEST with SolEdge2d-EIRENE and ERO2.0. *Physica Scripta*, T171:014013, 2020.

[28] http://www.eirene.de/trim.pdf.

[29] H. Volker. Pmi-2.1-t042-d001 - feasibility of demo particle exhaust part 3: Divertor configuration design guidelines. https://idm.euro-fusion.org/?uid=2pe9dp.

[30] C. Day, Y. Igitkhanov, S. Varoutis, and C. Tantos. Tfv-4.1-t16-d01 - report on tfv / divertor cross-topics aspects. https://idm.euro-fusion.org/?uid=2p2pzs.

[31] E. Kaveeva, V. Rozhansky, I. Senichenkov, E. Sytova, I. Veselova, S. Voskoboynikov, X. Bonnin, R. A. Pitts, A. S. Kukushkin, S. Wiesen, and D. Coster. SOLPS-ITER modelling of ITER edge plasma with drifts and currents. *Nuclear Fusion*, 60(4):046019, 2020-03.

[32] V. Kotov, D. Reiter, A. S. Kukushkin, H. D. Pacher, P. Brner, and S. Wiesen. Radiation absorption effects in b2-EIRENE divertor modelling. *Contributions to Plasma Physics*, 46(7-9):635–642, 2006-09.

[33] M. Carr, A. Meakins, and M. Tomes. cherab/core: Release v1.2.0. available online at: https://zenodo.org/record/3551871.

[34] R. C. Reid, J. M. Prausnitz, and T. K. Sherwood. *The properties of gases and liquids*. Mc-Graw-Hill, 1977.

[35] http://www.eirene.de/html/amjuel.html.

[36] http://www.eirene.de/html/hydhel.html.

Figures

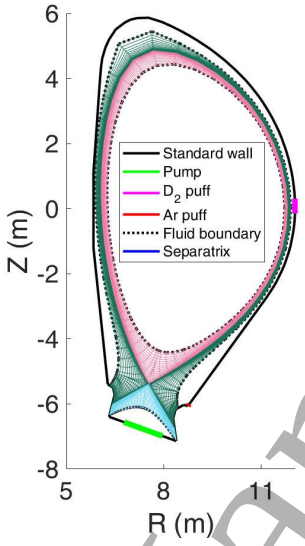

Figure 1a. Overview of the EU-DEMO first wall and divertor profile. For the sake of reference, the mesh used for plasma calculations in the present work is also shown.

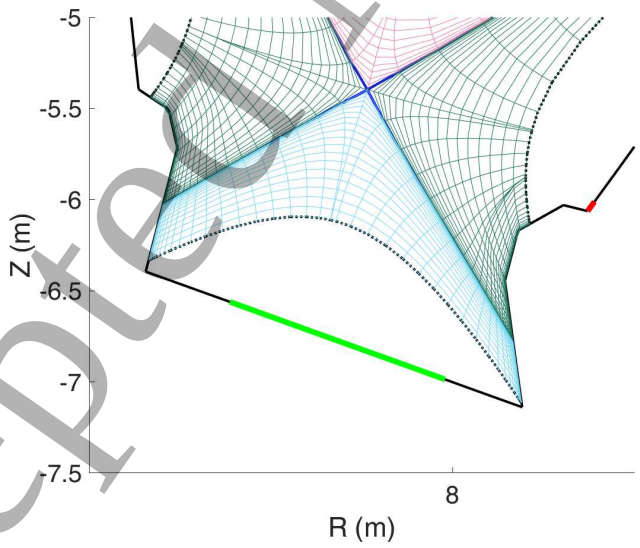

Figure 1b. Zoom of the divertor region. This makes visible the Ar puff location at the top of the buffer region

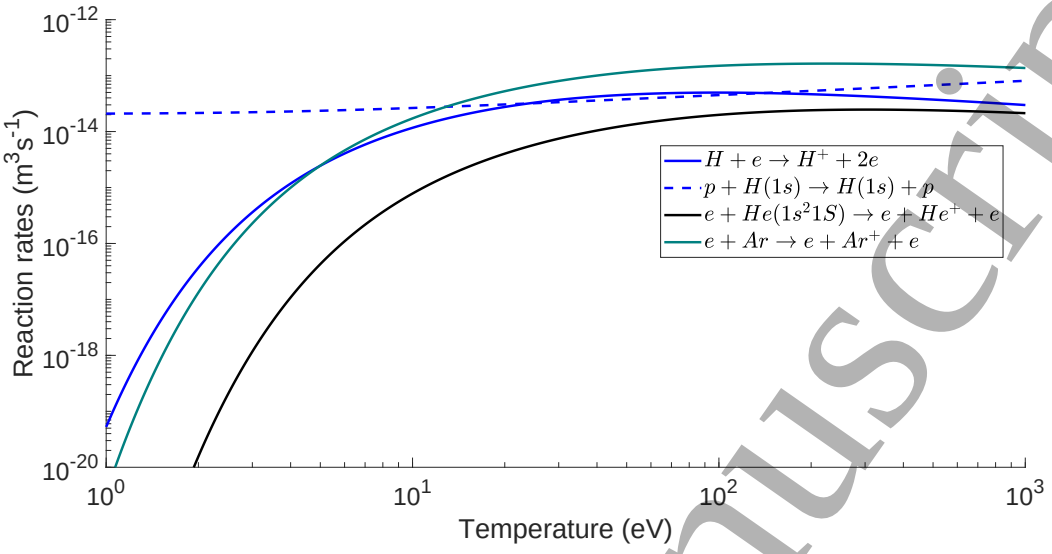

Figure 2a. Atomic physics reactions involving D, He and Ar atoms

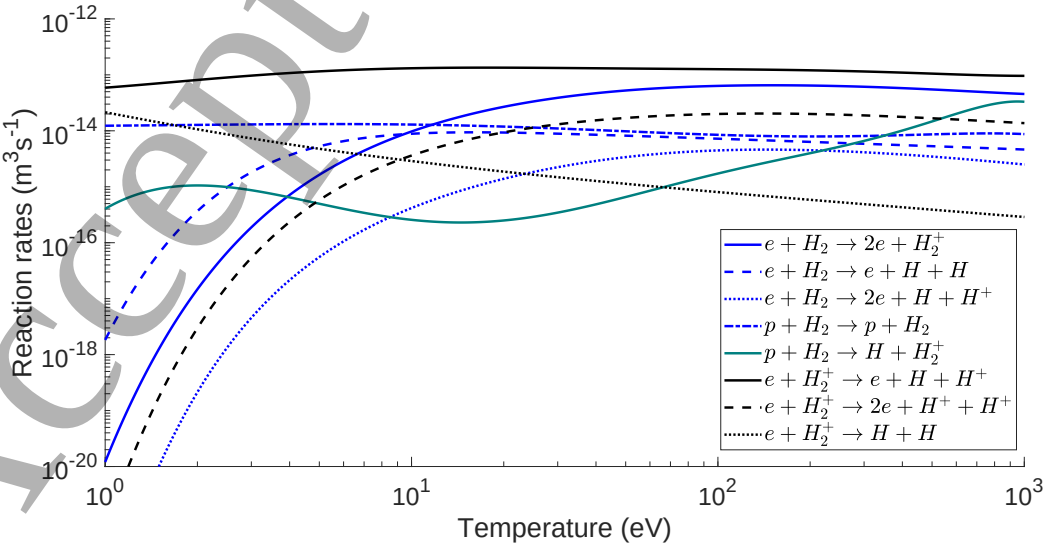

Figure 2b. Atomic physics reactions involving molecules

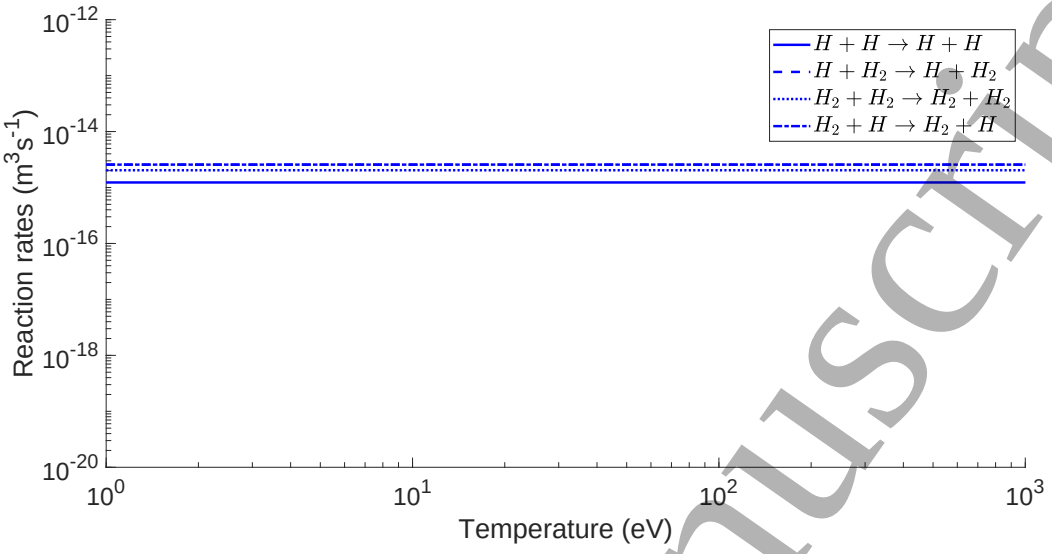

Figure 2c. Atomic physics reactions involving molecular ions

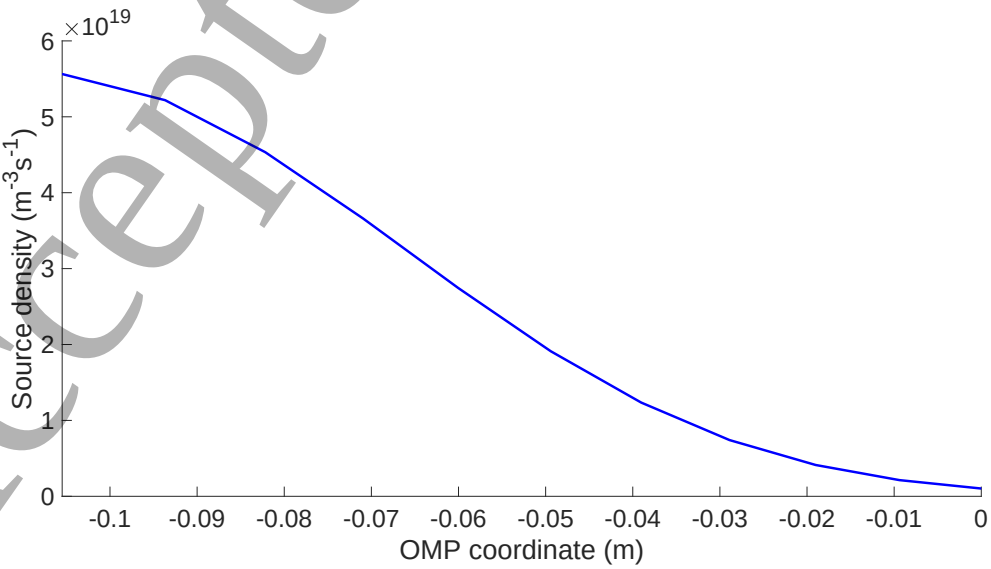

Figure 3. D volumetric pellet-like source profile in the core region

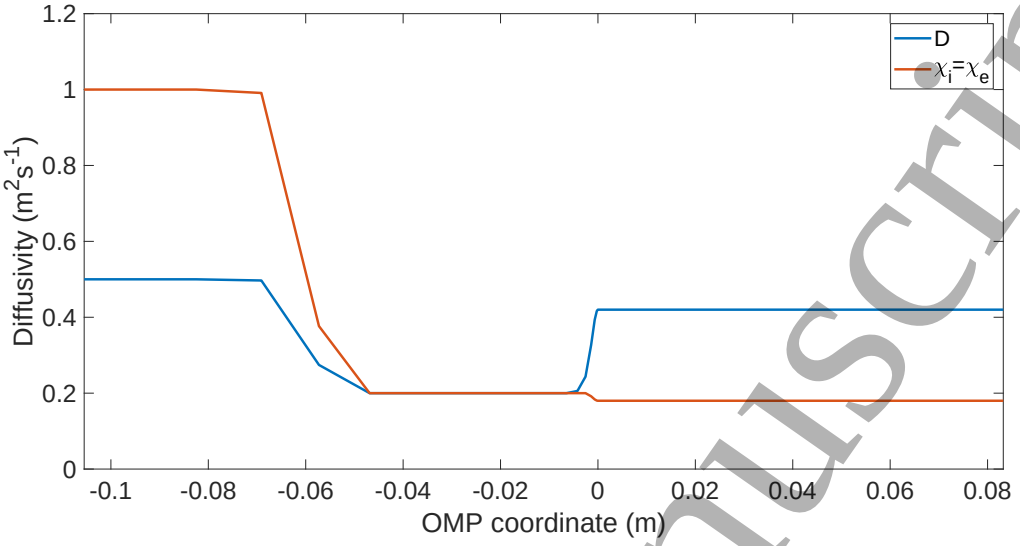

Figure 4. Transport coefficients used for the modeling described in this work.

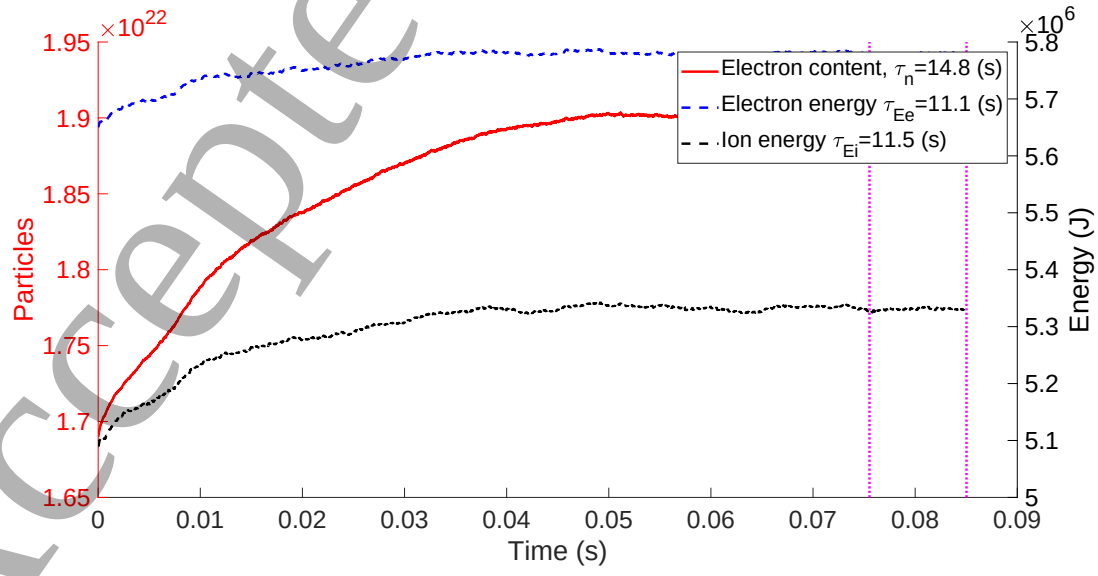

Figure 5. Evolution to steady state of global electron content (left axis) and electron/ion internal energy (right axis). The dotted magenta lines mark the time instants t_1 and t_2 taken to evaluate the characteristic evolution times.

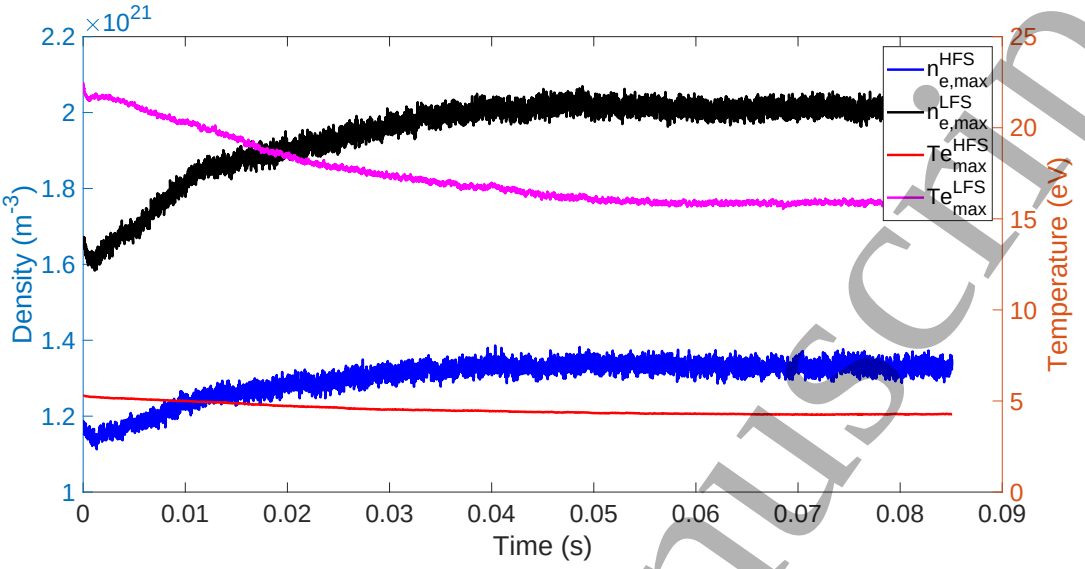

Figure 6. Evolution to steady state of selected local quantities. Left axis: maximum target densities. Right axis: maximum target electron temperatures. The black and magenta lines,

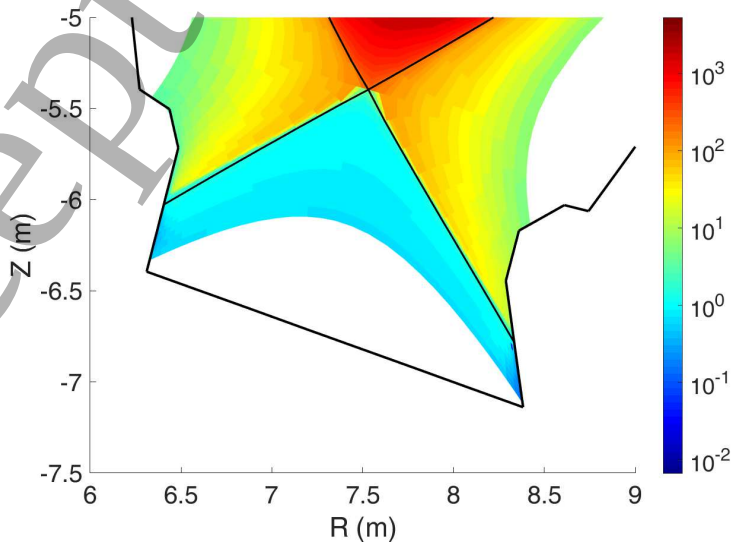

Figure 7a. Electron temperature map (eV) in the divertor region.

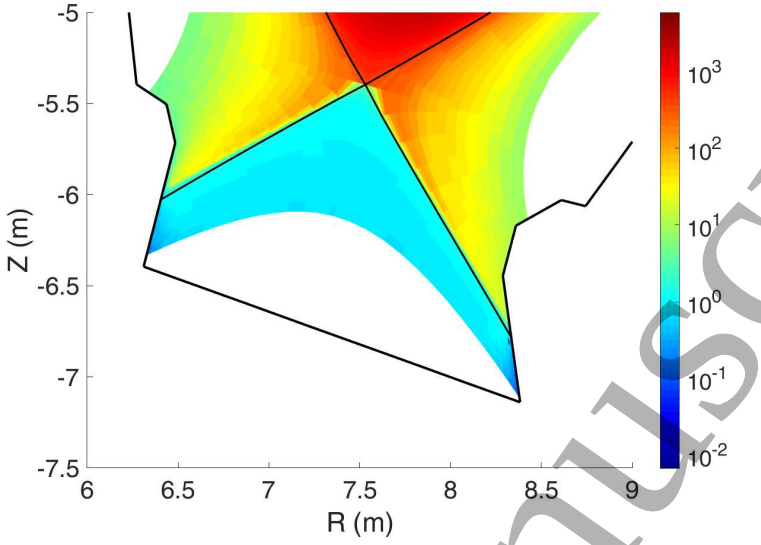

Figure 7b. Ion temperature map (eV) in the divertor region.

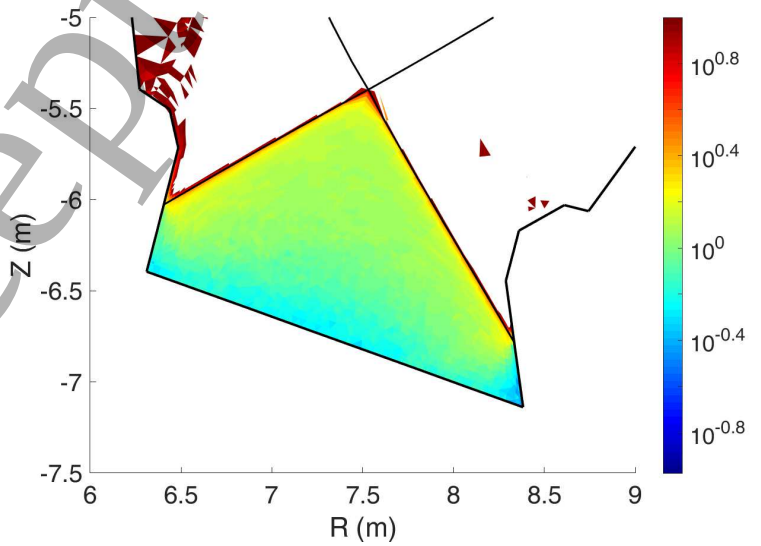

Figure 7c. Atomic D temperature map (eV) in the divertor region.

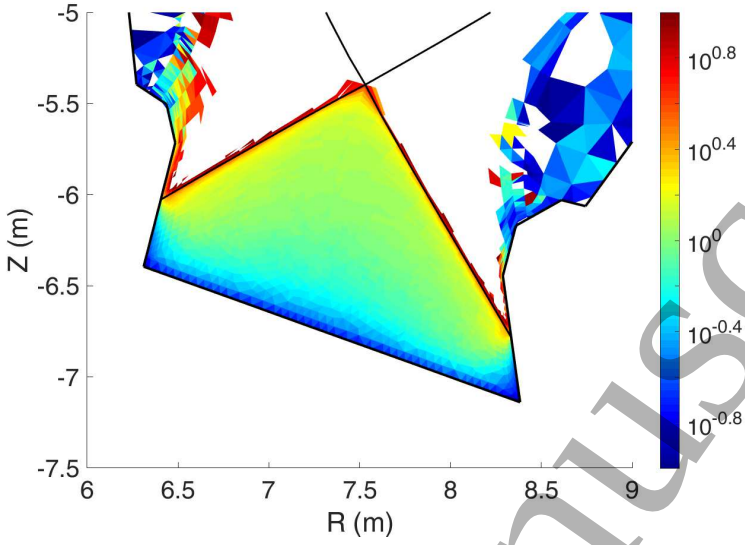

Figure 7d. Molecular D temperature map (eV) in the divertor region.

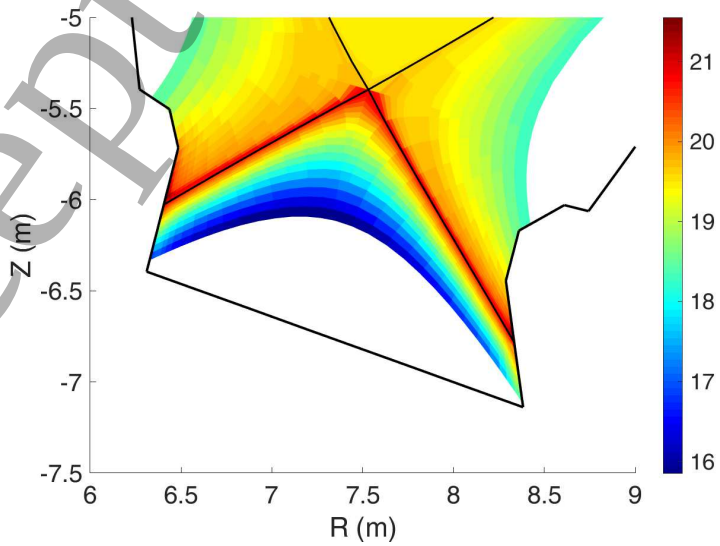

Figure 8a. Electron density in the divertor region (10^{-3}).

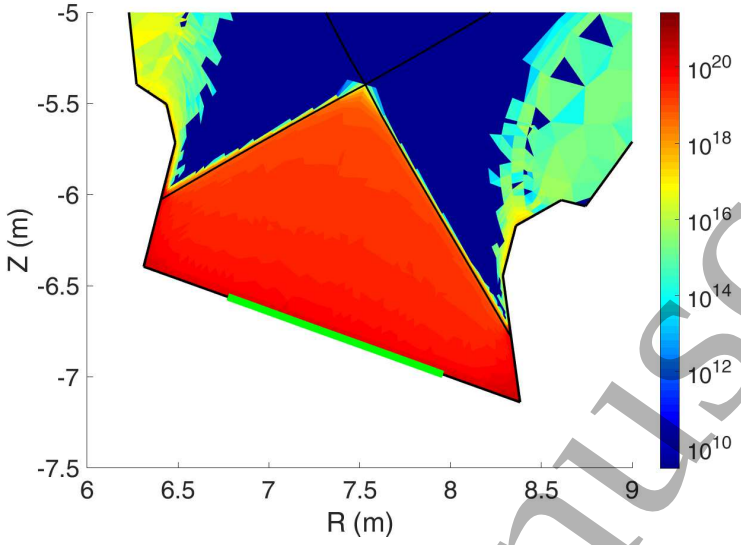

Figure 8b. Molecular neutral density in the divertor region (10^{-3}). The green line at the bottom of the divertor shows the opening of the pump duct.

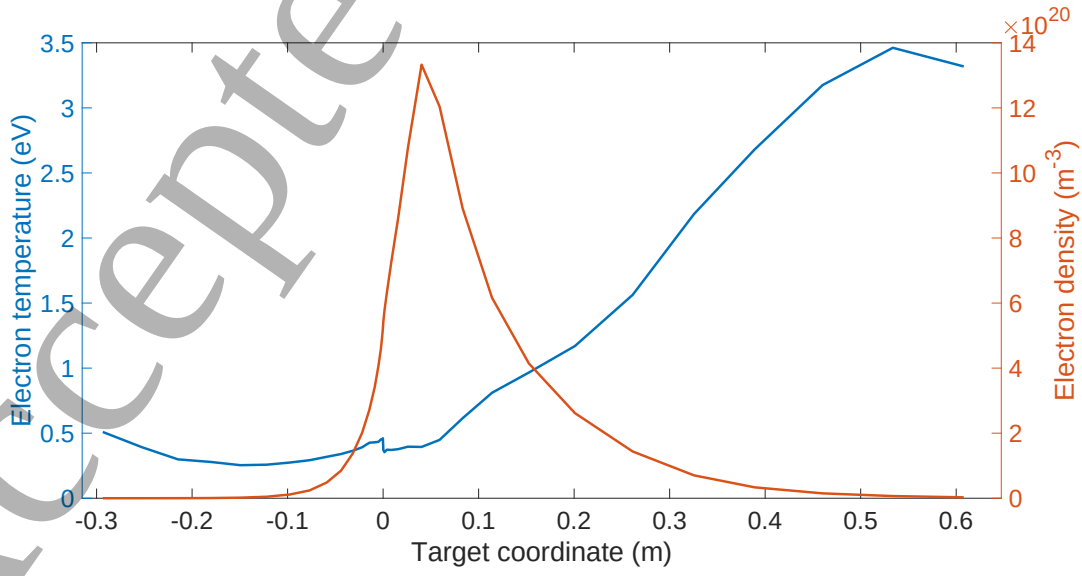

Figure 9a. Electron temperature and density along the HFS target. As discussed in the main text, the artifact visible close to the separatrix does not influence any of the results discussed in the paper.

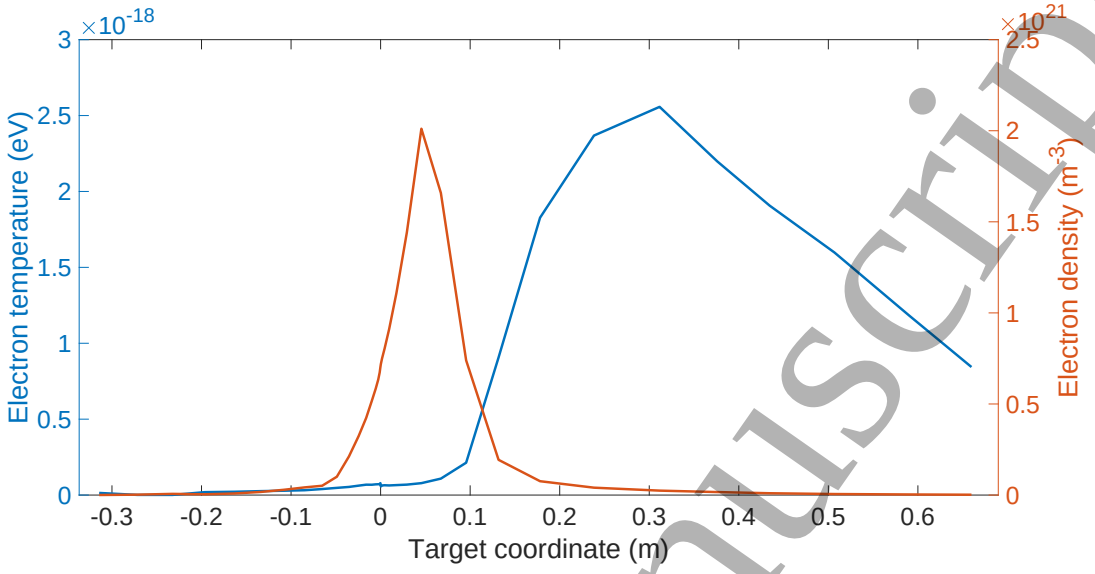

Figure 9b. Electron temperature and density along the LFS target

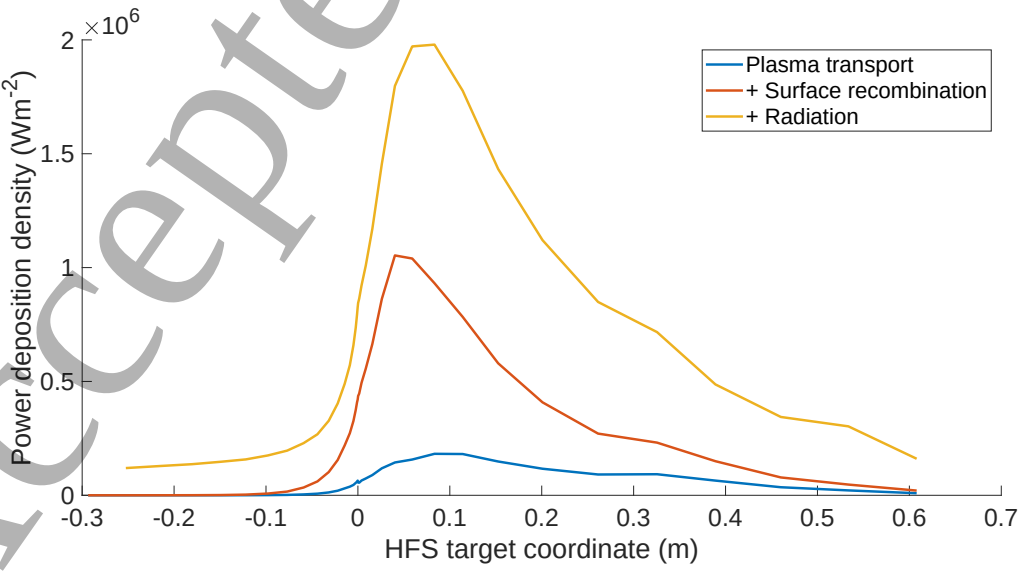

Figure 10a. Power deposition profile along the HFS target. Contribution from radiative processes was calculated with the CHERAB code [33].

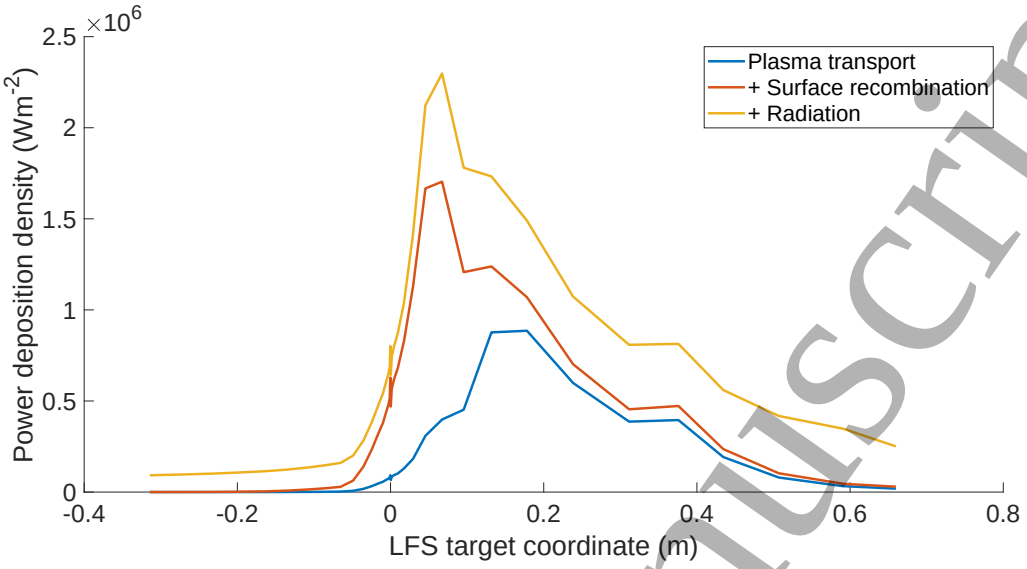

Figure 10b. Power deposition profile along the LFS target. Contribution from radiative processes was calculated with the CHERAB code [33]. As discussed in the main text, the artifact visible close to the separatrix does not influence any of the results discussed in the paper.

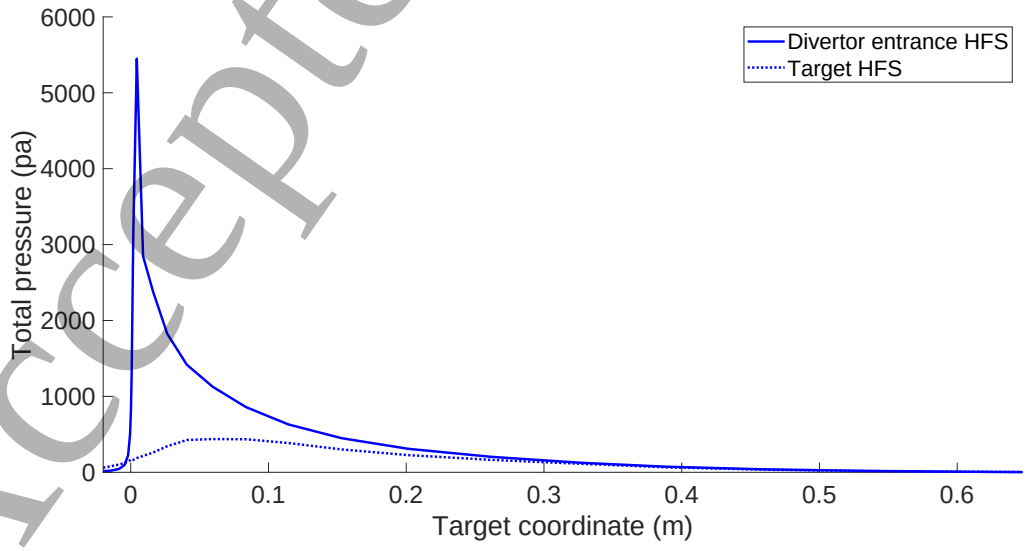

Figure 11a. Comparison of HFS p_e profiles at the divertor entrance (solid lines) and $2 \times p_e$ at the targets (dotted lines)

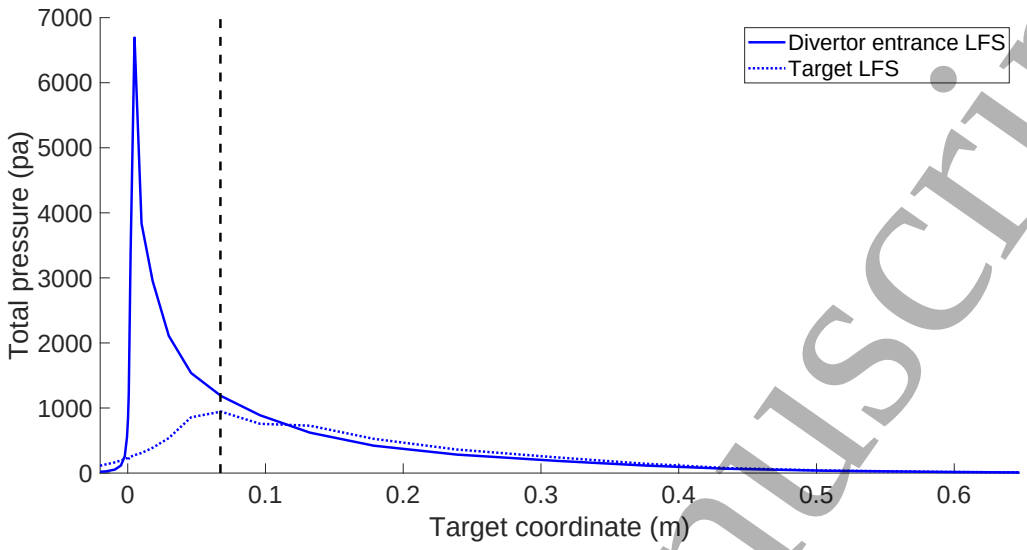

Figure 11b. Comparison of LFS p_e profiles at the divertor entrance (solid lines) and $2 \times p_e$ at the targets (dotted lines). The black dotted line shows the position of the maximum power density deposition on the target, taken from figure 10b.

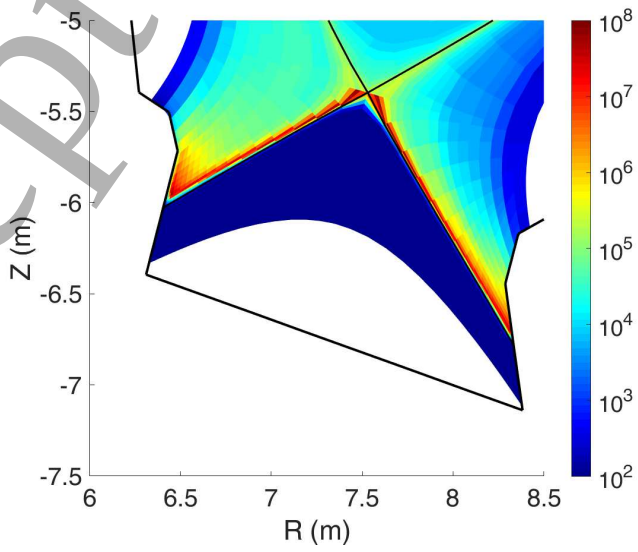

Figure 12. Radiative dissipation in the divertor region (W/m^3).

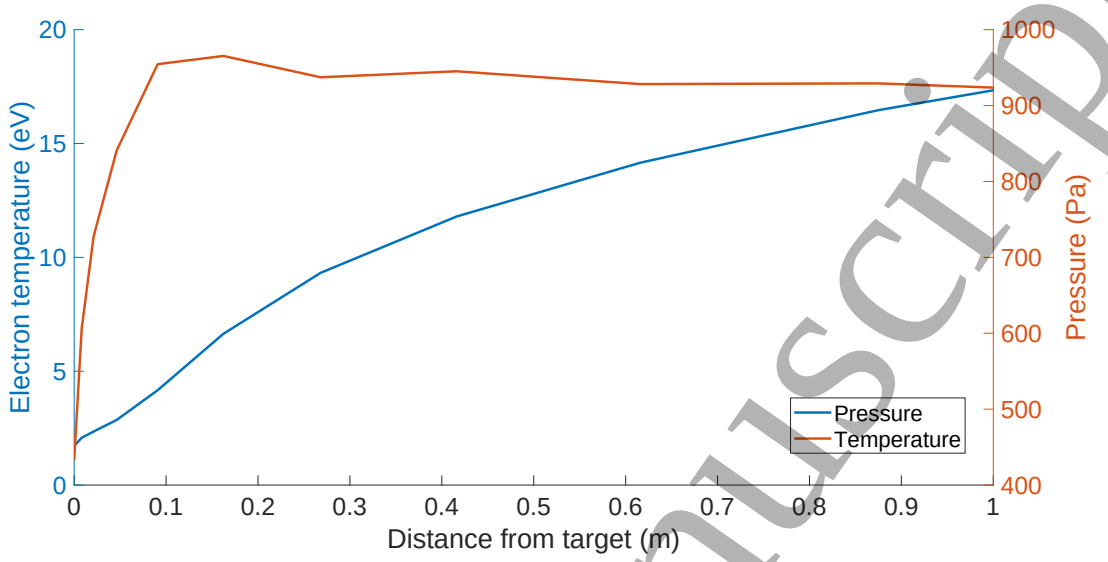

Figure 13a. Electron density and plasma temperature profiles along a selected flux tube.

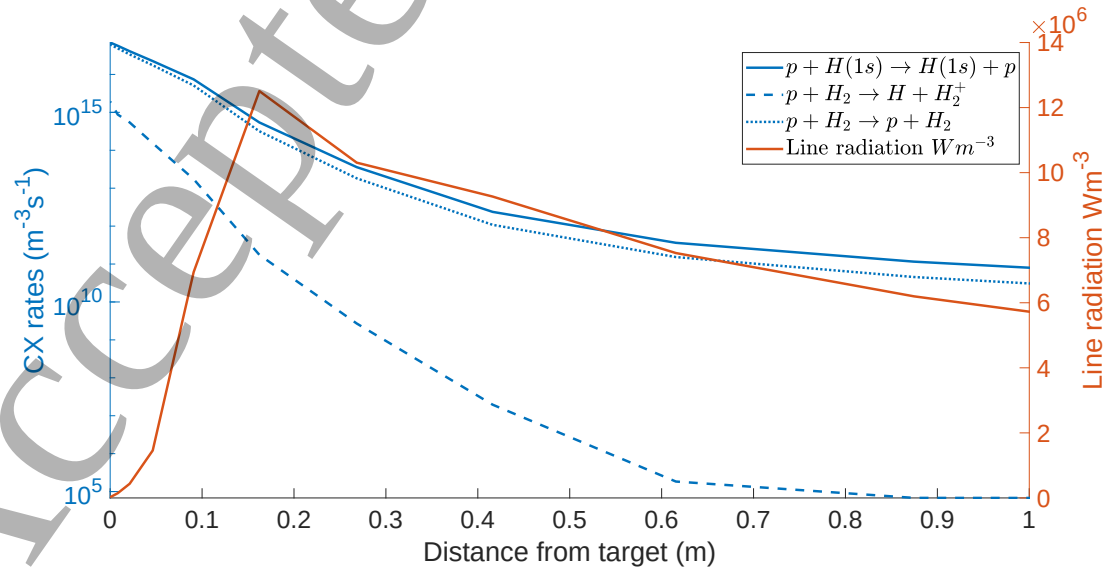

Figure 13b. Rate of CX exchange processes and line radiation density profiles along a selected flux tube.

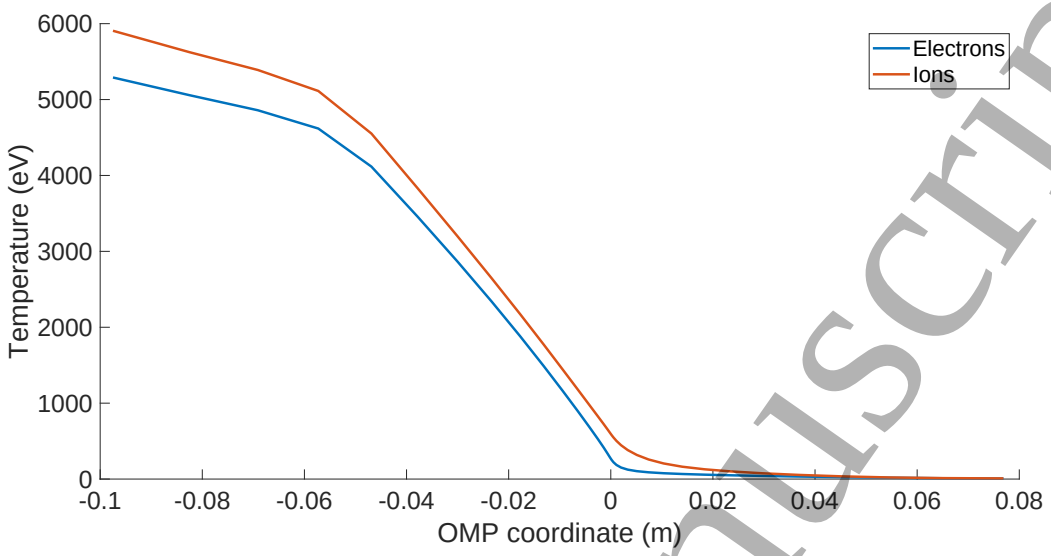

Figure 14. Core temperature profiles at the OMP

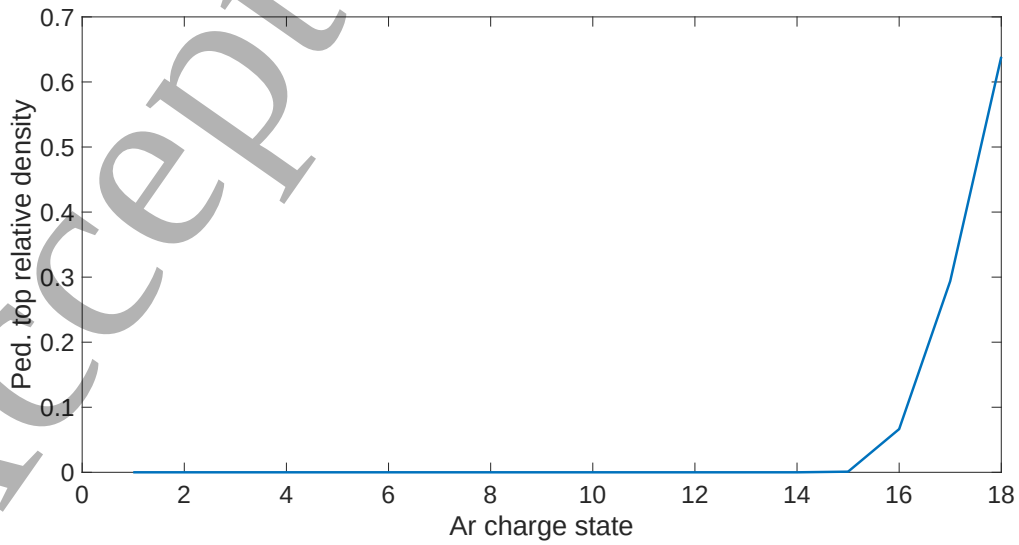

Figure 15. Distribution of Ar charge states at the core boundary

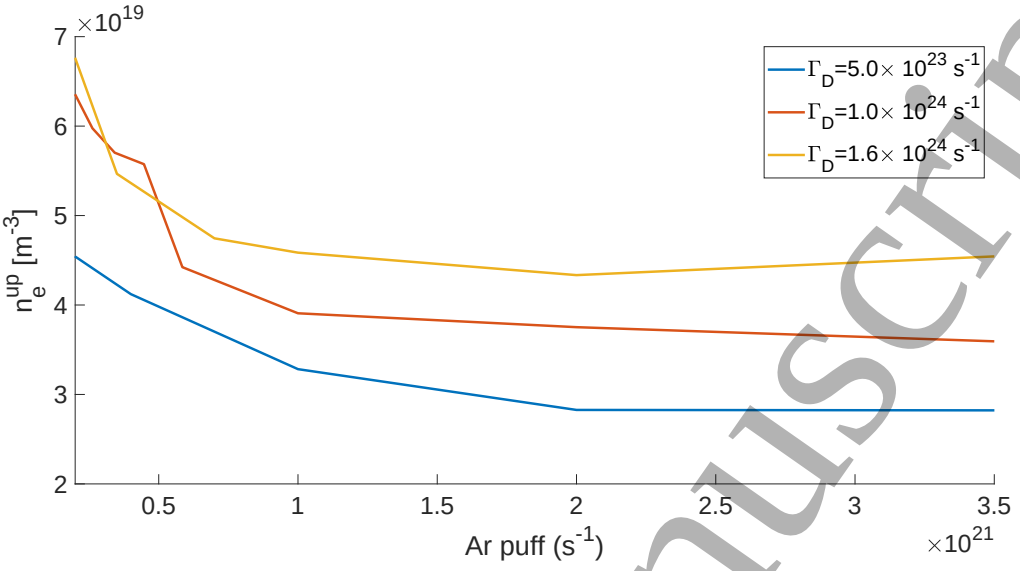

Figure 16a. OMP separatrix electron density for various Ar and D puff level (from a series of fluid runs)

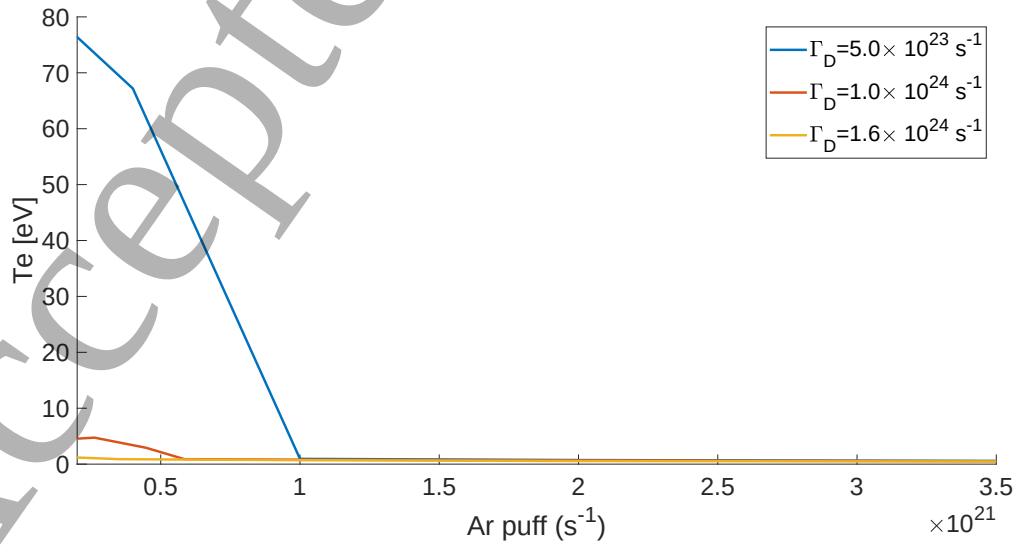

Figure 16b. Maximum outer target electron temperature for various Ar and D puff level (from a series of fluid runs)

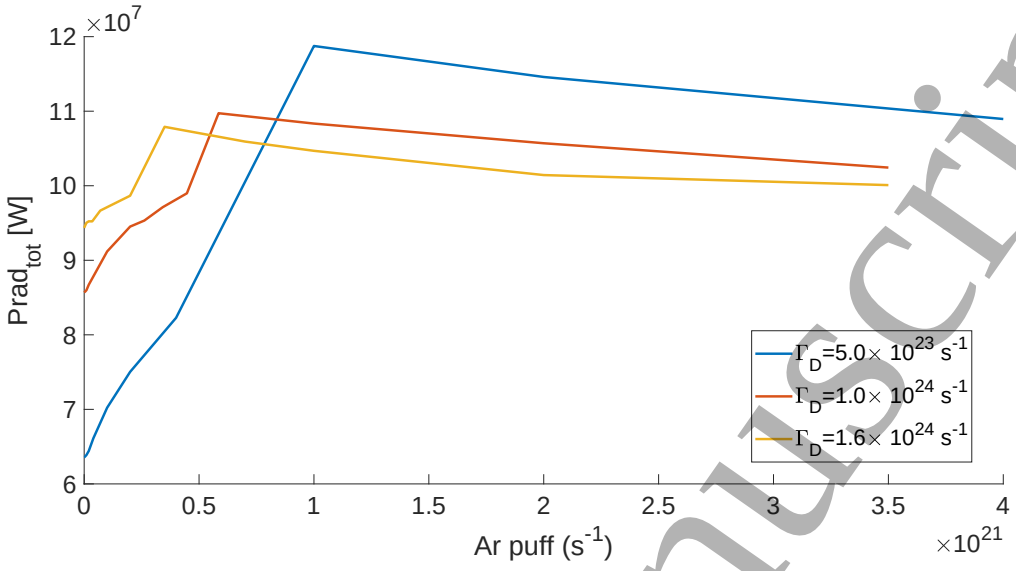

Figure 16c. Total line radiation for various Ar and D puff level (from a series of fluid runs)

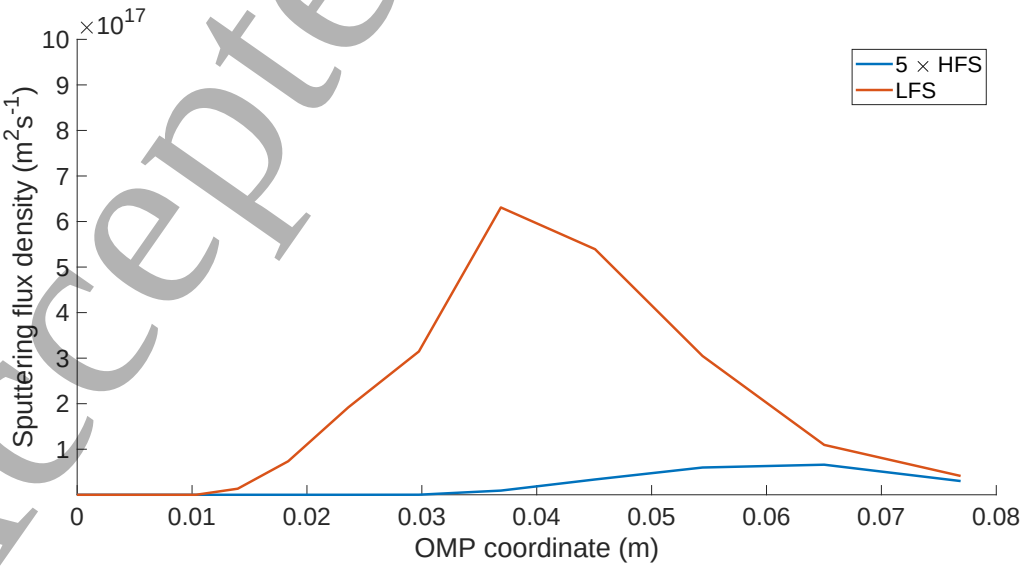

Figure 17a. Sputtering profiles along the targets. Data for HFS were multiplied by a factor of 5 to allow appreciating them on the figure scale.

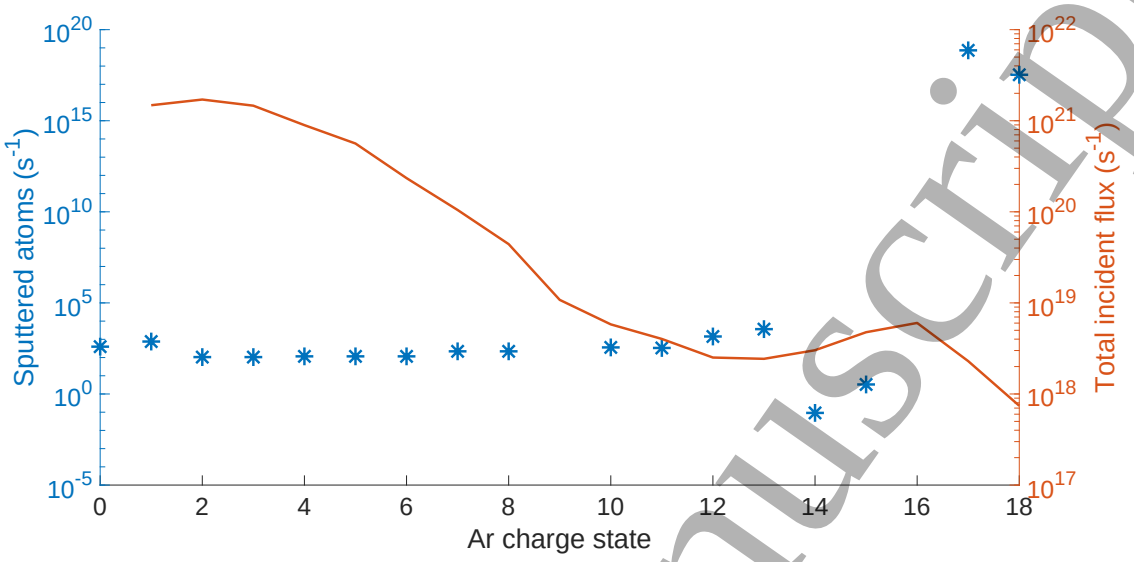

Figure 17b. LFS sputtering rate (left axis) and particle flux (right axis) vs. Ar ionzation state

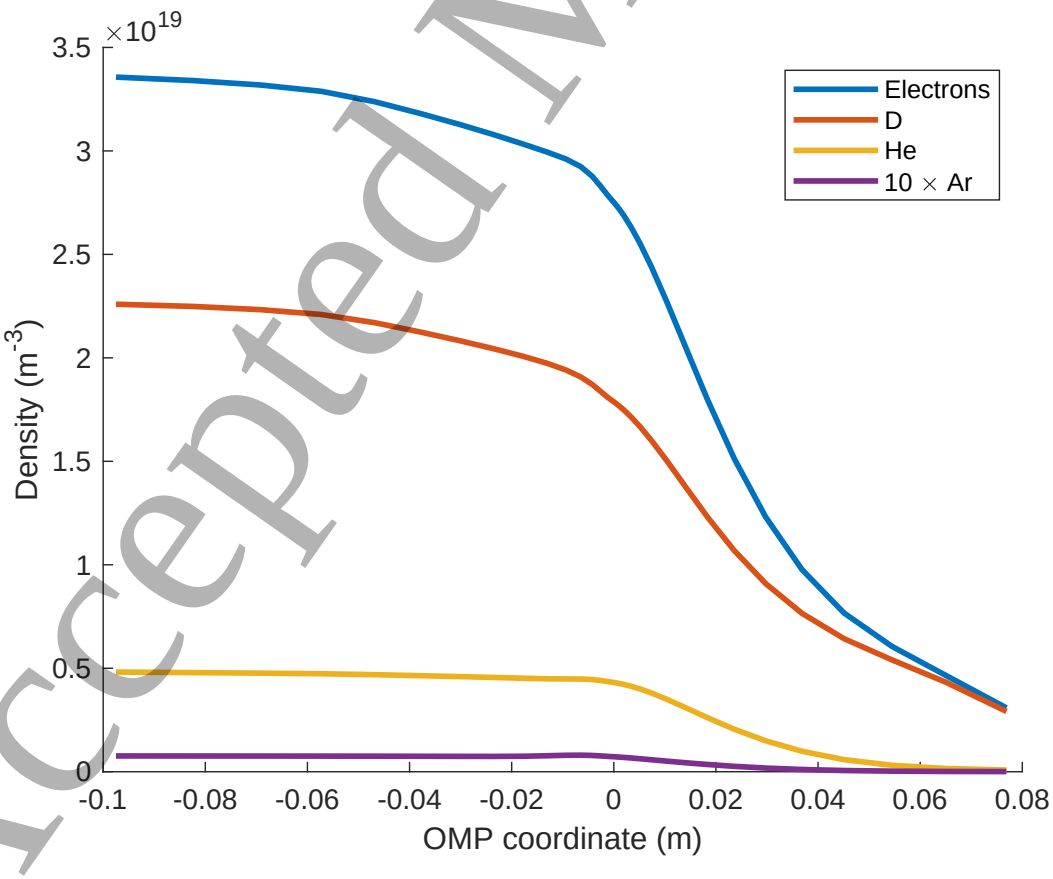

Figure 18. Core density profiles. Ar density was multiplied by a factor 10 to allow appreciating it on the same scale as D and He.

Tables

Group	Reaction	Source
Involving atoms	$H + e \rightarrow H^+ + 2e$	amjuel
	$p + H(1s) \rightarrow H(1s) + p$	hydhel
	$e + He(1s^2 1S) \rightarrow e + He^+ + e$	hydhel
	$e + Ar \rightarrow e + Ar^+ + e$	amjuel
Molecular reactions	$e + H_2 \rightarrow 2e + H_2^+$	amjuel
	$e + H_2 \rightarrow e + H + H$	amjuel
	$e + H_2 \rightarrow 2e + H + H^+$	amjuel
	$p + H_2 \rightarrow p + H_2$	amjuel
	$p + H_2 \rightarrow H + H_2^+$	amjuel
	$e + H_2^+ \rightarrow e + H + H^+$	amjuel
	$e + H_2^+ \rightarrow 2e + H^+ + H^+$	amjuel
	$e + H_2^+ \rightarrow H + H$	amjuel
Neutral-neutral collisions	$H + H \rightarrow H + H$	[34]
	$H + H_2 \rightarrow H + H_2$	[34]
	$H_2 + H_2 \rightarrow H_2 + H_2$	[34]
	$H_2 + H \rightarrow H_2 + H$	[34]

Table 1. List of atomic physics reactions included in the our model. For most reactions, data source are contained in the databases amjuel [35] or hydhel [36], distributed with the EIRENE package. Data for neutral-neutral reactions are derived from [34]

MDSPLUS ID	Γ_D (atoms/s)	Γ_{Ar} (atoms/s)	Usage
181738	5.00×10^{23}	1.50×10^{19}	Everywhere, except figures 16a-16c
182479	5.00×10^{23}	2.00×10^{20}	Figures 16a-16c
182484	5.00×10^{23}	4.00×10^{20}	Figures 16a-16c
182475	5.00×10^{23}	1.00×10^{21}	Figures 16a-16c
182480	5.00×10^{23}	2.00×10^{21}	Figures 16a-16c
182459	1.00×10^{24}	2.00×10^{20}	Figures 16a-16c
182463	1.00×10^{24}	2.62×10^{20}	Figures 16a-16c
182464	1.00×10^{24}	3.42×10^{20}	Figures 16a-16c
182467	1.00×10^{24}	4.47×10^{20}	Figures 16a-16c
182468	1.00×10^{24}	5.85×10^{20}	Figures 16a-16c
168836	1.00×10^{24}	1.00×10^{21}	Figures 16a-16c
168841	1.00×10^{24}	2.00×10^{21}	Figures 16a-16c
168848	1.00×10^{24}	3.50×10^{21}	Figures 16a-16c
158761	1.60×10^{24}	2.00×10^{20}	Figures 16a-16c
147216	1.60×10^{24}	3.50×10^{20}	Figures 16a-16c
147213	1.60×10^{24}	7.00×10^{20}	Figures 16a-16c
158762	1.60×10^{24}	1.00×10^{21}	Figures 16a-16c
158763	1.60×10^{24}	2.00×10^{21}	Figures 16a-16c
158764	1.60×10^{24}	3.50×10^{21}	Figures 16a-16c

Table 2. List of SOLPS-ITER runs used to produce this paper. Runs are uniquely identified via their ID in the MDSPlus database.